

Universal topological quantum computation with strongly correlated Majorana edge modes

Ye-Min Zhan^{1,2,3,*}, Yu-Ge Chen^{4,*}, Bin Chen⁵, Ziqiang Wang⁶, Yue Yu^{1,2,3,†} and Xi Luo^{5‡}

1. State Key Laboratory of Surface Physics, Fudan University, Shanghai 200433, China

2. Center for Field Theory and Particle Physics, Department of Physics, Fudan University, Shanghai 200433, China

3. Collaborative Innovation Center of Advanced Microstructures, Nanjing 210093, China

4. Institute of Physics, Chinese Academy of Sciences, Beijing 100190, China

5. College of Science, University of Shanghai for Science and Technology, Shanghai 200093, China

6. Department of Physics, Boston College, Chestnut Hill, MA 02467, USA

(Dated: March 23, 2022)

Majorana-based quantum gates are not complete for performing universal topological quantum computation while Fibonacci-based gates are difficult to be realized electronically and hardly coincide with the conventional quantum circuit models. In Ref. [1], it has been shown that a strongly correlated Majorana edge mode in a chiral topological superconductor can be decomposed into a Fibonacci anyon τ and a thermal operator anyon ε in the tricritical Ising model. The deconfinement of τ and ε via the interaction between the fermion modes yields the anyon collisions and gives the braiding of either τ or ε . With these braidings, the complete members of a set of universal gates, the Pauli gates, the Hadamard gate and extra phase gates for 1-qubit as well as controlled-not gate for 2-qubits, are topologically assembled. Encoding quantum information and reading out the computation results can be carried out through electric signals. With the sparse-dense mixed encodings, we set up the quantum circuit where the controlled-not gate turns out to be a probabilistic gate and design the corresponding devices with thin films of the chiral topological superconductor. As an example of the universal topological quantum computing, we show the application to Shor's integer factorization algorithm.

I. INTRODUCTION

The idea of quantum computation can be traced back to the 1980s by Manin, Benioff, and Feynman et al., who tried to simulate the quantum world by coherent quantum states and quantum models [2–4]. In the 1990s, Shor's integer factorization algorithm provides a theoretical example of the applications of quantum computation, which has an enormous advantage over its classical counterpart [5]. Nowadays, the realizations and applications of quantum computation have become one of the most frontier topics in the developments of quantum technology [6]. In the attempts of constructing the prototypes of quantum computers, there have been proposals based on the entangled states of photons [7], superconducting circuits [8], bound states in cold atoms [9] or optical lattices [10], quantum wells [11], quantum dot spins [12], single spins in diamonds [13], Bose-Einstein condensates [14], rare-earth atoms [15], and carbon nanospheres [16]. Though quantum computing provides promising applications in quantum simulation, data mining, machine learning, deciphering, artificial intelligence, etc., the road to realizing the quantum computation remains tough. In the theoretical side, besides predicting material realizations, another serious challenge lies in making the quantum computation universal, i.e., to realize a protocol for universal quantum computation based on quantum sys-

tems and quantum logic gates such as the controlled-not (CNOT) gate. While in the experimental side, one serious challenge is the decoherence between the quantum states and the environment which will cause errors. For example, to create an error-tolerant logic gate for a singlet logic qubit, more than 150 physical logic gates are needed when processing in Steane codes [17, 18].

A. Topological Quantum Computation

Recent progresses on topological quantum states of matter have shed new light on overcoming these obstacles. The concept of topological quantum computation (TQC) was first proposed by Kitaev [19, 20], which is believed to be fault-tolerant due to the protection of the topological gap between the system and the environment. The computational data is stored non-locally by the topological excitations, namely, anyons. In the TQC, the initial data is prepared by coherent many-particle anyon states. The braidings between anyons generate unitary transformations that correspond to logic gates and the readout of the results are achieved by fusing the anyons into observable quantities [21].

The concept of anyon was proposed by Leinaas and Myrheim [22], and Wilczek [23]. Laughlin pointed out that the quasi-particles with fractional charge in the fractional quantum Hall effects (FQHE) could be anyons. In the $\nu = 5/2$ even denominator FQHE, Moore and Read noticed that the non-Abelian anyons are of Ising type [24, 25]. Later, Freedman et al. proved that to achieve universal quantum computation, the topological quan-

*These two authors contribute equally.

†Correspondence to: yuyue@fudan.edu.cn

‡Correspondence to: xiluo@usst.edu.cn

tum gates with these Ising type non-Abelian anyons alone are not enough, and additional non-topological phase gates, e.g., the $\frac{\pi}{8}$ gate, are needed [26]. Among the possible non-Abelian anyon systems, the Fibonacci anyon is the simplest case for achieving universal TQC [20], which is likely to exist in FQHE with $\nu = 12/5$ [27, 28], but there are substantial uncertainties. A recent study reported the possibility that the Fibonacci anyon appears in the $\nu = \frac{2}{3}$ FQHE, appropriately proximitized by a superconductor [29, 30]. But this requires the survival of the superconductivity in a strong magnetic field.

Besides FQHE, Kitaev proposed Majorana bound states at the two ends of topological superconducting quantum wires [31]. Two Majorana zero modes (MZMs) at the two ends have a $\pi/2$ phase shift. They correspond to the "real" and "imaginary" part of a non-local fermion. Except for the phase difference, the higher dimensional non-Abelian representations of the braid group of the MZMs are equivalent to the Ising type anyons' [32–34]. Some quantum gates for TQC can be achieved by exchanging the Majorana bound states in so-called T-junctions [34]. Unfortunately, the MZMs also suffer from lacking of topological phase gates for universal TQC. Even so, Kitaev's seminal work has stimulated the physicists' enthusiasm for finding MZMs. Using the proximity effect of the *s*-wave superconductor, Fu and Kane proposed a theory for MZM in the superconducting vortex at the interface between an *s*-wave superconductor and a topological insulator [35]. There are other proposals for MZMs in semiconductor heterostructures [36], semiconductor-superconductor heterostructures [37], superconductor/2D-topological-insulator/ferromagnetic-insulator hybrid system [38], and so on. Besides the progresses on the theories, there are also lots of experimental reports on MZMs. Midgap states at zero bias voltage were observed in indium antimonide nanowires in a magnetic field [39–43]. Although the results are consistent with the existence of MZMs [37], the zero energy states can also be explained by other non-topological trivial bound states [44]. Possible MZMs were observed at the ferromagnetic atomic chains on a superconductor [45], but there can be other explanations besides MZM. A strong indirect evidence for MZM was observed in $\text{Bi}_2\text{Te}_3/\text{NbSe}_2$ heterostructure [46, 47]. A $2e^2/h$ conductance was observed in InSb nanowire, which is believed to be an evidence for MZM [48], but this result was retracted. And the authors' latest data show more possible interpretations besides MZM [49]. Recently, the evidences of MZMs are reported in iron-based superconductors, such as $\text{FeTe}_{0.55}\text{Se}_{0.45}$ [50–52], $(\text{Li}_{0.84}\text{Fe}_{0.16})\text{OHFeSe}$ [53], LiFeAs [54], and $\text{CaKFe}_4\text{As}_4$ [55], as well as the Majorana vortex states in iron-based superconducting nanowires [56], and MZM are also reported in atomically Fe-based Yu-Shiba-Rusinov chains [57–59], which provide new materials for creating Ising type topological quantum computer [60].

The MZMs in FQHE with $\nu = 5/2$ and Kitaev's model are closely related to the vortex bound states and chi-

ral Majorana edge modes (χ MEMs) in the *p*-wave superconductor [61]. The interior of a vortex can be regarded as vacuum with a χ MEM moving along the edge of the vortex, and when the radius of the vortex goes to zero, the χ MEM reduces to the MZM, i.e., this provides a duality between MZM and MEM. Therefore, the *p*-wave topological superconductor is an important candidate for realizing the TQC. Although the material realization of the *p*-wave superconductor has not been found yet, for example, Sr_2RuO_4 , which remains controversial [62, 63], the materials with effective *p*-wave superconductivity are possible to construct. One possible scenario is by using the *s*-wave superconductor/quantum anomalous Hall heterostructure, and the proximity effect will induce a chiral topological superconducting (χ TSC) phase [64, 65]. Furthermore, the braiding of the MEMs are carried automatically when propagating along the edge, and the $e^2/2h$ conductance is believed to be a smoking gun signal for the existence of MEM [65]. Unfortunately, the experimental evidences of this scenario remain controversial [68–70]. The reason is that in this heterostructure, there can be residual metallic states in the quantum anomalous Hall substrate, which can also explain the half quantized conductance [69]. And the MZMs in the vortices of the superconducting area will dramatically change the results of the braiding [71, 72].

We have briefly review the recent progresses in the TQC, especially for those based on Majorana objects. For more recent subject review, see [73]. We can classify these Majorana-based TQC proposals into two approaches to the non-Abelian statistics: (1) For one species Majorana fermion system, the many-particle wave functions of Majorana fermions obey the Abelian statistics. Other degrees of freedom such as the vortices must exist to have non-Abelian statistics, e.g, in the $\nu = 5/2$ fractional quantum Hall states and the Ising model [24, 32] as well as the edge chiral vortices approach [74]. This kind of Majorana fermion systems can do the TQC but not universal by braiding solely. (2) For two species Majorana fermion model which is we consider here, no further degrees of freedom such as vortices are necessary. The two species Majorana fermions may be non-Abelian when the fermion number conservation is reduced to the fermion parity (FP) conservation, e.g., in superconductors. This approach has been used in [31–34, 64, 65]. This kind of Majorana fermion systems also cannot be used to do universal quantum computation by braiding solely. In Appendix A, we give more explanations to these two approaches for readers' convenience.

B. The Goal and Main Results of This Work

We already know that there are TQC processes with two types of non-Abelian anyons. The Fibonacci anyon-based one is universal but restricted by realistic materials. The algorithm is also different from the conventional quantum circuit models. On the other hand, the Ma-

Majorana fermion-based one is relevant to practical physical systems and the quantum circuit models, but is not universal by braiding solely. Furthermore, there should be no other low-energy fermionic or apparently even no bosonic states in the system to avoid the Majorana modes overlapping effectively, which is another obstacle for Majorana fermion-based TQC [66, 67]. The main goal of this article is to design quantum gates for the universal TQC consistent with the quantum models, which combines the advantages of the χ MEMs and the Fibonacci anyons.

In a recent work concerns Fibonacci topological superconductor [1], the authors showed that, in 7-layers of χ TSC, the interacting χ MEMs γ_a ($a = 1, \dots, 7$) whose conformal dimension is $\frac{1}{2}$ may be thought as composite objects: $\gamma_a = \tau_a \varepsilon_a$ where τ is the Fibonacci anyon with the conformal dimension $\frac{2}{5}$ and ε is a thermal operator with the conformal dimension $\frac{1}{10}$ in the tricritical Ising (TCI) model. The validity of such a composition is guaranteed by the coset factorization of the conformal field theory (CFT): $SO(7)_1 = (G_2)_1 \times \text{TCI}$ [75]. (For readers' convenience, we briefly list the basic facts of G_2 in Appendix B.)

The components of the MEMs can be delocalized when two MEMs with opposite chirality interact through a special interacting potential [1]. We here will analyze this interaction and show that it can be expressed as the interacting potential between charged fermions which consist of the MEMs when they meet in the interacting domains. Furthermore, the interaction between two propagating MEMs yields the collisions of either two τ or two ε . When the collided τ and ε are recombined, the braidings of anyons are achieved, similar to the Laughlin anyons collision [76].

With these anyons and their braidings, we obtain:

(1) These braidings cause the fractional statistical angles θ and then give the topological θ -phase gates with $\theta = \frac{\pi}{4}, \frac{\pi}{10}$ and $\frac{2\pi}{5}$. With the $\frac{\pi}{4}$ -phase gate and the braiding gate by braiding two MEMs in different pairs of the χ MEMs [65], the Pauli- X, Y, Z gates, the H gate, and the CNOT gate can be created. The other two phase gates, the $\frac{\pi}{10}$ - and $\frac{2\pi}{5}$ -phase gates, which are topological, can replace the $\frac{\pi}{8}$ -phase gate. With the similar method in [78], we prove that all these gates form a set of universal gates. We then can design a universal TQC with quantum circuit model [79].

(2) We find that encoding quantum information and reading out the computation results can be carried out through electric signals.

(3) The quantum gates are generally dependent on the FP, the even or odd of the fermion number of the quantum state in the process, which is conserved and then determined by the initial qubits. For example, for a device set up by fixed physical elements of a phase gate, the 1-qubit initial state with odd FP gives a phase gate $\text{diag}(1, i)$ while it is $\text{diag}(-i, 1)$ for even FP. A device gives

the CNOT gate if the 2-qubits are of an odd FP but it does not give a CNOT for the FP even qubits and vice versa, which is discussed in more details.

(4) Therefore, for a given physical device, side measurements are needed in order to have the input state with correct FP for the designed gate. The side measurement requires additional MEMs besides those in the computing state space. It is known that to encode the Majorana-based n logic qubits, $2n + 2$ Majorana bound states or MEMs are needed [32]. However, with the side measurements, $4n$ MEMs are required to encode the n -qubits [80]. The former is usually called the dense encoding process while the latter is the sparse encoding one [80]. Using the dense encoding only is not convenient to build a quantum circuit which is applied to well-known quantum algorithms, e.g., the quantum Fourier transformation and Shor's integer factorization algorithm. Thus, the sparse encoding will be used to build our quantum circuit. However, in the sparse encoding, one can only prepare qubits in superposition states, but no entanglement states with braiding only [81]. For instance, with the sparse encoding, we cannot realize the CNOT gate from two 1-qubits. It has to be realized in the dense encoding. Thus, our process is a mixed one with the sparse-dense encodings. Notice that because of the no entanglement rule, the FP measurements are needed. Therefore, our CNOT gate is still probabilistic, although the efficiency is improved.

Using this process, we may realize a quantum circuit for Shor's algorithm. Since there is one-to-one correspondence between the quantum gates and the designed devices with the χ TSC thin films, we can design a universal TQC for the large integer primary factorization.

C. Paper's Organization

This paper is organized as follows: In Sec. II, we review a 7-layer TSC system and the corresponding conformal field theory properties. In Sec. III, we study the interaction between the right- and left- χ MEMs (R, L - χ MEMs) when they meet. In Sec. IV, we show the anyon exchange and braiding due to the interaction between the χ MEMs. In Sec. V, we construct a set of universal topological gates which are used to encode a universal TQC. The corresponding physical devices are designed. In Sec. VI, we show that the computing results can be output by electric signals. In Sec. VII, we use these quantum gates to build the quantum circuit with the sparse-dense mixed encoding. We apply these designations to the quantum Fourier transformation, Toffoli gate which is the key element for an adder, and then the quantum circuit for Shor's algorithm. In Sec. VIII, we give the device designation of the quantum circuits by using the elements of the quantum gates which consist of the thin films of the χ TSC and the interacting domains of the MEMs. The last section devotes to our conclusions. We have six appendices to support the results obtained in the main

text.

II. MULTILAYER χ TSC SYSTEMS

We consider multilayers of χ TSC which are separated layer-by-layer by the trivial insulator. Spinless or spin polarized charged fermions are injected into the edges of the multilayers and each edge fermion is decomposed into two MEMs with different species: $\psi = \frac{1}{\sqrt{2}}(\gamma^{(1)} + i\gamma^{(2)})$ (See Appendix A). Depending on the multilayer assignment, we label γ_a the MEM into the a th layer. We do not explicitly index the species of the MEM because each of them freely runs in its own layer edge. Thus, a χ MEM on the edge of each layer is spatially separated from the other χ MEMs. We denote the edge coordinate as x . The free χ MEMs $\gamma_a^{R,L}(x)$ on the edges of an individual layer is described by the Hamiltonian

$$H_a^{R,L} = \pm \frac{iv}{2} \gamma_a^{R,L} \frac{\partial}{\partial x} \gamma_a^{R,L}, \quad (1)$$

where \pm are corresponding to the *right* (R)- and *left* (L)-chirality. The N -layer χ MEMs are described by the $\text{SO}(N)_1$ CFT [1]. The fermion number N of the system is not conserved but the even and odd of the fermion number, i.e., the FP $(-1)^N$, is conserved.

For our purpose, we take $N = 7$. It is known that if there are appropriate interactions between the MEMs (see below and Appendix C), the $\text{SO}(7)_1$ CFT can be factorized by the coset $\text{SO}(7)_1/(\text{G}_2)_1$. The central charge of the Wess-Zumino-Witten models of a level k affine Lie group G is given by $c_G = \frac{k \dim g}{k+g}$ where $\dim g$ is the dimension of the Lie algebra and g is the dual Coxeter number. For $\text{SO}(7)_1$, $c = \frac{21}{1+5} = \frac{7}{2}$ while $c = \frac{14}{1+4} = \frac{14}{5}$ for $(\text{G}_2)_1$. Therefore, the central charge of the coset $\text{SO}(7)_1/(\text{G}_2)_1$ is $\frac{7}{2} - \frac{14}{5} = \frac{7}{10}$. This means that the CFT of the Wess-Zumino-Witten model of the coset $\text{SO}(7)_1/(\text{G}_2)_1$ is nothing but the TCI model [75]. The $(\text{G}_2)_1$ CFT has one type of anyon: Fibonacci τ with the conformal dimension $h_\tau = \frac{2}{5}$ while the $\text{SO}(7)_1/(\text{G}_2)_1$ CFT is equivalent to the TCI model where non-Abelian anyons, the thermal operators ε and ε' have the conformal dimensions $h_\varepsilon = \frac{1}{10}$ and $h_{\varepsilon'} = \frac{3}{5}$, respectively [75]. These non-Abelian anyons have the same quantum dimensions, i.e., $d_\tau = d_\varepsilon = d_{\varepsilon'} = \frac{1+\sqrt{5}}{2}$. Thus, as we have mentioned in *Introduction*, the MEMs can be decomposed into $\gamma_a = \tau_a \varepsilon_a$ in terms of the coset construction due to the adaptation of the conformal dimensions.

III. INTERACTION BETWEEN R- AND L- χ MEMS FOR 7-LAYERS

Formally, the seven free χ MEMs Hamiltonian $H^{R,L} = \sum_{a=1}^7 H_a^{R,L}$ can be decomposed into $H_{G_2}^{R,L} + H_{TCI}^{R,L}$. The explicit expressions of $H_{G_2}^{R,L}$ and $H_{TCI}^{R,L}$ can be found in [1] and are not important here, but we know that

$[H_{TCI}^{R,L}, J_{R,L}^\alpha] = 0$ where the current operators $J_{R,L}^\alpha$ ($\alpha = 1, \dots, 14$) are defined by $J_{R,L}^\alpha = \frac{1}{2} \sum_{a,b} \Xi_{ab}^\alpha \gamma_a^{R,L} \gamma_b^{R,L}$ for Ξ^α being the generators of the fundamental representation of G_2 . Following Ref. [1], we consider the interaction between the R - and L - χ MEMs as

$$H_i = -\lambda \sum_{\alpha=1}^{14} J_{R,L}^\alpha. \quad (2)$$

Using the quadratic Casimir operator of G_2 (see Eq. (B3)), H_i is rewritten as [1]

$$H_i = -\frac{\lambda}{3} \sum_{a \neq b} \gamma_a^R \gamma_b^R \gamma_b^L \gamma_a^L - \frac{\lambda}{3} \sum' \gamma_a^R \gamma_b^R \gamma_c^L \gamma_d^L, \quad (3)$$

where \sum' means the summation runs over the indices with $\epsilon_{abcdefg} \hat{f}_{efg} = -1$ (see Appendix B). If any two MEMs with different species but the same chirality meet, they become a local charged fermion, say, $\psi_{ab}^R = \frac{1}{2}(\gamma_a^{R(1)} + i\gamma_b^{R(2)})$ and $\psi_{ab}^L = \frac{1}{2}(\gamma_a^{L(1)} + i\gamma_b^{L(2)})$ in Fig. 1 (e). Since $i\gamma_a^{R(1)} \gamma_b^{R(2)} = 2n_{ab}^R - 1 = 2\tilde{n}_{ab}^R$ with the fermion number operator $n_{ab}^R = \psi_{ab}^{R\dagger} \psi_{ab}^R$, for $\lambda > 0$, the interaction Hamiltonian becomes the interactions with a particle-hole symmetry between the charged fermions

$$H_i = U \sum_{a \neq b} \tilde{n}_{ab}^R \tilde{n}_{ba}^L + U \sum' \tilde{n}_{ab}^R \tilde{n}_{cd}^L, \quad (4)$$

where $U = \frac{4\lambda}{3}$. If two MEMs with different species and chirality meet (Fig. 1(f)), the Hamiltonian can be expressed as

$$H_i = U \sum_{a \neq b} \tilde{n}_{aa}^{RL} \tilde{n}_{bb}^{RL} + U \sum' \tilde{n}_{ad}^{RL} \tilde{n}_{bc}^{RL}, \quad (5)$$

where $\tilde{n}_{ad}^{RL} = n_{ad}^{RL} - \frac{1}{2}$ for the fermion number operator $n_{ad}^{RL} = \psi_{ad}^{RL\dagger} \psi_{ad}^{RL}$ with $\psi_{ad}^{RL} = \frac{1}{2}(\gamma_a^{R(1)} + i\gamma_d^{L(2)})$, and so on. Therefore, it is possible to realize the interactions, e.g., by introducing four narrow stripes of the χ TSC sample from the edges of the thin films to a domain where the MEMs interact (See Appendix C). In reality, the coupling constant λ may be dependent on the domains. But if the strengths of these coupling constants are of the same order, these differences are not relevant at the strong coupling fixed point. The τ -anyon in the domain gains an energy gap $\Delta \sim e^{-\pi v/2\lambda}$ for $\lambda > 0$ [1]. This means that in the strong coupling region (see the green box in Figs. 1(a,b)), τ are reflected by this interaction potential while ε are transmitted. In this sense, the composite MEMs in the interacting domains are decomposed into spatially separated τ and ε . Notice that the interactions $\gamma_a^R \gamma_b^R \gamma_b^L \gamma_d^L$ with $a \neq b \neq d$, etc will gap ε . Therefore, when introducing the MEMs to the interacting domains, one must avoid this type of interactions. The FP is also conserved after the interaction is switched on.

IV. ANYON BRAIDING

In Fig. 1 (a) and (b), we depict two ways that a R - χ MEM and a L - χ MEM propagate to the interacting domain. In both cases, $\varepsilon_{R,L}$ are transmitted while $\tau_{R,L}$ are reflected by the interacting potential, but τ_R and τ_L exchange in Fig. 1 (a) while $\varepsilon_R, \varepsilon_L$ exchange in Fig. 1(b). These anyon exchanges give rise to the fractional statistics by braiding the anyons [76]. The world lines of the corresponding anyon braidings are shown in Fig. 1 (c) and (d), respectively. The reason for why there are two types of collisions can be traced to the fact that we have two ways to write the four-Majorana fermion interaction in Eq. (4). Figs. 1 (e) and (g) are the examples of the interacting processes corresponding to τ 's braiding while Figs. 1 (f) and (h) are to ε 's braiding.

For a CFT, the four-point correction function corresponding to the anyons collision can be calculated if we assume the τ is reflected with a ratio $r \sim 1 - e^{-\Delta/T}$ and the ε is fully transmitted according to the interaction Eq. (2). By a Wick rotation $y \rightarrow it$, the collision matrices for Fig. 1 can be determined by the following 8-point Green's function

$$\begin{aligned} & \langle \tau(z_{1\tau}) \varepsilon(z_{1\varepsilon}) \tau(z_{2\tau}) \varepsilon(z_{2\varepsilon}) \tau(z_{3\tau}) \varepsilon(z_{3\varepsilon}) \tau(z_{4\tau}) \varepsilon(z_{4\varepsilon}) \rangle \\ & \propto \langle \tau(z_{1\tau}) \tau(z_{2\tau}) \tau(z_{3\tau}) \tau(z_{4\tau}) \rangle \langle \varepsilon(z_{1\varepsilon}) \varepsilon(z_{2\varepsilon}) \varepsilon(z_{3\varepsilon}) \varepsilon(z_{4\varepsilon}) \rangle \end{aligned}$$

with $z_{a\tau} \rightarrow z_{a\varepsilon}$ for $z = x + iy$ because of the coset decomposition of $SO(7)_1$ CFT. The 4-point correlation function of a primary field ϕ in the CFT can be exactly calculated [77]

$$\langle \phi(z_1) \phi(z_2) \phi(z_3) \phi(z_4) \rangle = F(x) (z_{12} z_{13} z_{14} z_{23} z_{24} z_{34})^{-2h/3}, \quad (6)$$

where $z_{ij} = z_i - z_j$ and $x = \frac{z_{12} z_{34}}{z_{13} z_{24}}$. The function $F(x)$ can be determined by the Ward identities of the CFT. Exchanging any two ϕ fields, we have a statistical phase $e^{2ih\pi}$ (where we have taken $e^{-i\pi} = -1$ for convenience). Wick rotating back, braiding τ or ε obtains a statistical phase $e^{4i\pi/5}$ or $e^{i\pi/5}$. In the following we assume τ is completely reflected while ε is fully transmitted. In reality, the finite temperature will cause an error with probability proportional to $e^{-\Delta/T}$ in τ collision while the interaction deviating from (2) can cause the error both for τ and ε collisions.

We now want to design the topological phase elements. Fig. 2 (a) is the schematics of the elements $G(\theta) = e^{-2i\theta}$. Fig. 2 (e) is the top view of Fig. 2 (a) when the two interacting domains are different (The other two cases are shown in Appendix D). A charged spinless fermion ψ is injected from the lead to the 2-layer χ TSC such that $\psi \rightarrow \frac{1}{\sqrt{2}}(\gamma_1 + i\gamma_2)$ where the χ MEMs $\gamma_{1,2}$ run along the edges of layer 1 and 2, respectively. They then become the R and L - χ MEMs and enter one of the edge channels in 7-layers with an equal probability. The MEMs are factorized into anyons: $\gamma_{1,2} = \tau_{1,2}\varepsilon_{1,2}$. In the yellow interacting domain, anyons, say τ from Fig. 2 (e),

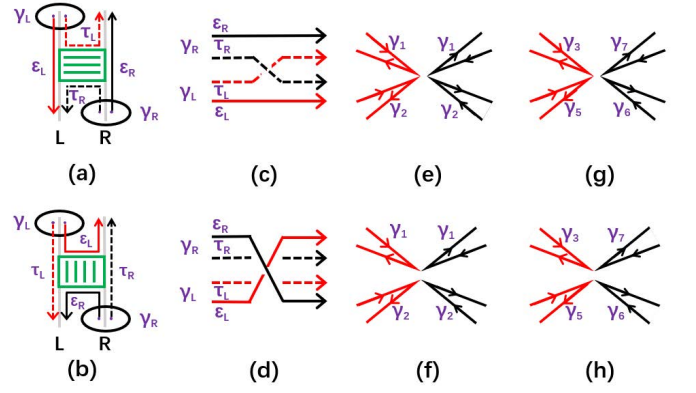


FIG. 1: (Color online) The illustrations of the anyon interactions, exchanges and braidings. The lines in the greens box in (a) and (b) stands for the interacting barrier for the τ -anyons while the ε -anyons are free from the barrier. (a) The τ s exchange. (b) The ε s exchange. (c) and (d): The braiding world lines of the anyons that correspond to (a) and (b), respectively. (e), (f), (g) and (h): Several examples of the interactions with the solid line being the edge of the χ TSC and the lower index in γ being the layer index. (e) $\tilde{n}_{12}^L \tilde{n}_{21}^R$, (f) $\tilde{n}_{11}^L \tilde{n}_{22}^R$, (g) $\tilde{n}_{35}^L \tilde{n}_{67}^R$, and (h) $\tilde{n}_{37}^L \tilde{n}_{56}^R$.

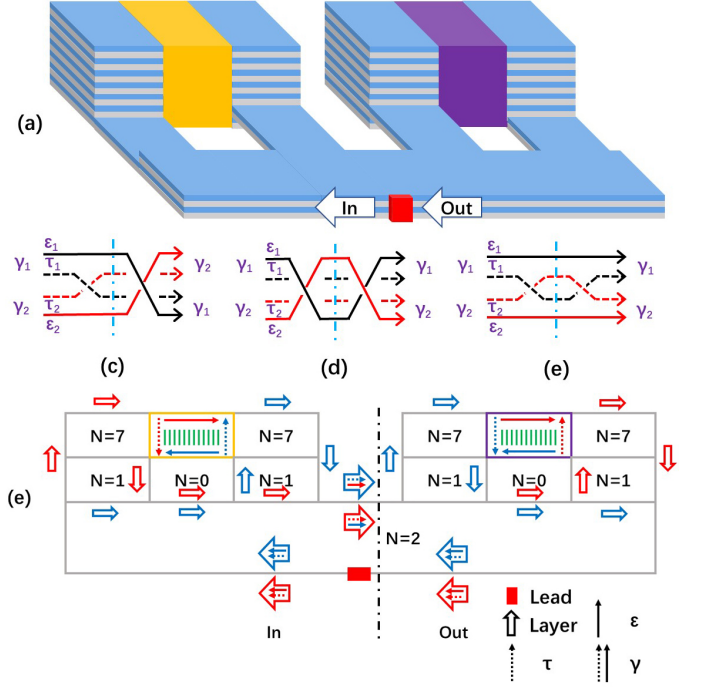


FIG. 2: (Color online) The setup of the element $G(\theta)$. (a) The device setup with the orange and purple parts being the interacting domains. The blue parts are the TSC thin films while the grey parts are the trivial insulator films. The red slab is the lead connected to external metal or to the other element in the TSC quantum circuit. (b), (c), and (d): The world lines between the in and out states, which represent $G(-\frac{\pi}{4})$, $G(\frac{\pi}{10})$ and $G(\frac{2\pi}{5})$, respectively. (e) The top view of the device for $G(-\frac{\pi}{4})$.

collide. This yields the braiding of τ . After the first collision, anyons run into the next 1-2-7 layer hybrid and collide in the purple domain. As a result, e.g., ε anyons braid. According to the anyon's conformal dimensions, the braiding of them causes statistical phases: $\tau_1 \rightarrow \tau_2, \tau_2 \rightarrow e^{i\frac{4\pi}{5}}\tau_1$ and $\varepsilon_1 \rightarrow \varepsilon_2, \varepsilon_2 \rightarrow e^{i\frac{\pi}{5}}\varepsilon_1$. The element $G(\theta)$ makes the anyons exchange twice: According to the world line in Fig. 2 (b), exchanging τ and ε in turn gives $G(-\frac{\pi}{4})$, i.e.,

$$\begin{aligned} \tau_1\varepsilon_1 + i\tau_2\varepsilon_2 &\rightarrow \tau_2\varepsilon_1 + ie^{i\frac{4\pi}{5}}\tau_1\varepsilon_2 \rightarrow \tau_2\varepsilon_2 + ie^{i\frac{4\pi}{5}}\tau_1e^{i\frac{\pi}{5}}\varepsilon_1 \\ &= \tau_2\varepsilon_2 - i\tau_1\varepsilon_1 = -i(\tau_1\varepsilon_1 + i\tau_2\varepsilon_2). \end{aligned} \quad (7)$$

This corresponds to $\gamma_1 \rightarrow \gamma_2, \gamma_2 \rightarrow -\gamma_1$ or $\gamma_{1,2} \rightarrow e^{-i\frac{\pi}{2}}\gamma_{1,2}$. Exchanging ε twice gives $G(\frac{\pi}{10})$, as shown in Fig. 2(c),

$$\begin{aligned} \tau_1\varepsilon_1 + i\tau_2\varepsilon_2 &\rightarrow \tau_1\varepsilon_2 + i\tau_2(e^{i\frac{\pi}{5}}\varepsilon_1) = \tau_1\varepsilon'_1 + i\tau_2\varepsilon'_2 \\ &\rightarrow \tau_1\varepsilon'_2 + i\tau_2e^{i\frac{\pi}{5}}\varepsilon'_1 = e^{i\frac{\pi}{5}}(\tau_1\varepsilon_1 + i\tau_2\varepsilon_2). \end{aligned} \quad (8)$$

This corresponds to $\gamma_a \rightarrow e^{i\frac{\pi}{5}}\gamma_a$. Exchanging τ twice gives $G(\frac{2\pi}{5})$ (Fig. 2(d)) and corresponds to $\gamma_a \rightarrow e^{i\frac{4\pi}{5}}\gamma_a$. Notice that $G(\frac{\pi}{4}) = (G(-\frac{\pi}{4}))^3$; $G(\frac{2\pi}{5}) = (G(\frac{\pi}{10}))^4$; $G(-\frac{\pi}{10}) = (G(\frac{\pi}{10}))^9$; and $G(-\frac{2\pi}{5}) = (G(\frac{\pi}{10}))^6$, and so on.

V. UNIVERSAL SET OF TOPOLOGICAL QUANTUM GATES

We now design a new set of topological quantum gates with these topological elements. Due to the FP conservation, the Hilbert space with a fixed FP for a single charged fermion is one-dimensional and then cannot encode a qubit. To construct a 1-qubit with a fixed FP, two charged fermion are required.

A. The Basic Braiding gates and Hadamard Gate for 1-Qubit

We consider charged fermions inject into the edges of two layer χ TSC thin films from leads in the terminals A and B (Fig. 3). The initial states are then $|n_A n_B\rangle$ for $n_{A,B} = 0, 1$ corresponding to the FP even and odd. If we consider weak current limit, we assume $n_{A,B} = 0, 1$ are the fermion number and the state $|1_A\rangle = \psi_A|0\rangle = \frac{1}{\sqrt{2}}(\gamma_1 + i\gamma_2)|0\rangle$ and $|1_B\rangle = \psi_B|0\rangle = \frac{1}{\sqrt{2}}(\gamma_3 + i\gamma_4)|0\rangle$. The basis of the initial state space is then given by

$$\{|0_A^{\gamma_1\gamma_2}0_B^{\gamma_3\gamma_4}\rangle, |0_A^{\gamma_1\gamma_2}1_B^{\gamma_3\gamma_4}\rangle, |1_A^{\gamma_1\gamma_2}0_B^{\gamma_3\gamma_4}\rangle, |1_A^{\gamma_1\gamma_2}1_B^{\gamma_3\gamma_4}\rangle\}.$$

The first and fourth ones form 1-qubit with the FP even while the other 1-qubit has the FP odd. We now braid two of MEMS while keeping the other two run straightforwardly. The basis of the final state spaces are transformed as

$$\{|0_C^{\gamma_2\gamma_1}0_D^{\gamma_3\gamma_4}\rangle, |0_C^{\gamma_2\gamma_1}1_D^{\gamma_3\gamma_4}\rangle, |1_C^{\gamma_2\gamma_1}0_D^{\gamma_3\gamma_4}\rangle, |1_C^{\gamma_2\gamma_1}1_D^{\gamma_3\gamma_4}\rangle\},$$

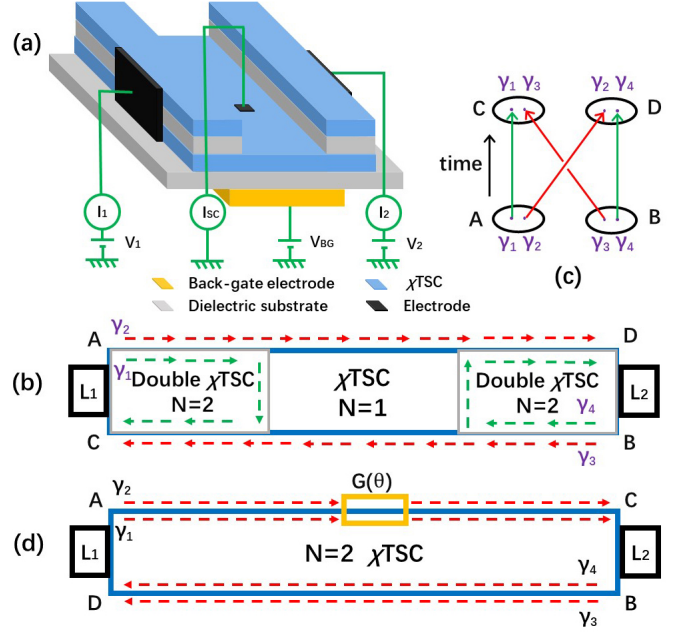


FIG. 3: (Color online) The device for the basic braiding gates. (a) A schematic of a layered χ TSC structure for the gate B_{23} . The black slabs are the leads, and the blue and grey ones are the same as those in the Fig. 2(a). The yellow slab is a back-gate electrode used to adjust the electric potential with a back-gate voltage when measuring the output data. (b) The top view of the device in (a). The arrows stand for the χ MEMS. (c) The world line of the MEMS. (d) The device schematic of the phase gate. The yellow sticker stands for the phase gate $G(\theta)$.

$$\{|0_C^{\gamma_1\gamma_3}0_D^{\gamma_2\gamma_4}\rangle, |0_C^{\gamma_1\gamma_3}1_D^{\gamma_2\gamma_4}\rangle, |1_C^{\gamma_1\gamma_3}0_D^{\gamma_2\gamma_4}\rangle, |1_C^{\gamma_1\gamma_3}1_D^{\gamma_2\gamma_4}\rangle\},$$

$$\{|0_C^{\gamma_1\gamma_2}0_D^{\gamma_4\gamma_3}\rangle, |0_C^{\gamma_1\gamma_2}1_D^{\gamma_4\gamma_3}\rangle, |1_C^{\gamma_1\gamma_2}0_D^{\gamma_4\gamma_3}\rangle, |1_C^{\gamma_1\gamma_2}1_D^{\gamma_4\gamma_3}\rangle\},$$

which correspond to braiding $(\gamma_1, \gamma_2), (\gamma_2, \gamma_3)$, and (γ_3, γ_4) , respectively. For a fixed FP, there are braiding matrices which transform the initial states to the final states, e.g., the braiding matrix for braiding γ_2 and γ_3 for the FP odd state is given by

$$\begin{pmatrix} |0_C^{\gamma_1\gamma_3}1_D^{\gamma_2\gamma_4}\rangle \\ |1_C^{\gamma_1\gamma_3}0_D^{\gamma_2\gamma_4}\rangle \end{pmatrix} = B_{23}^{(-)} \begin{pmatrix} |0_A^{\gamma_1\gamma_2}1_B^{\gamma_3\gamma_4}\rangle \\ |1_A^{\gamma_1\gamma_2}0_B^{\gamma_3\gamma_4}\rangle \end{pmatrix}. \quad (9)$$

And also we can define all $B_{ab}^{(\pm)}$ for $a < b = 1, \dots, 4$, where \pm stands for the FP of the qubit. Lian et al. gave a proposal for the gate $B_{23}^{(-)}$ with a quantum anomalous Hall insulator/superconductor proximity structure [65].

We here use the layered χ TSC structure for $B_{23}^{(-)}$ (Fig. 3(a)). As shown in Fig. 3(b), in the edges of the upper layer, γ_1 runs from A to C while γ_4 from B to D while in the edges of the lower layer, γ_2 runs from A to D while γ_3 from B to C . This yields the braiding between γ_2 and γ_3 (Fig. 3(c)). Under a braiding operation $\gamma_2 \rightarrow \gamma_3, \gamma_3 \rightarrow -\gamma_2$, the evolution of the FP odd state is thus equivalent

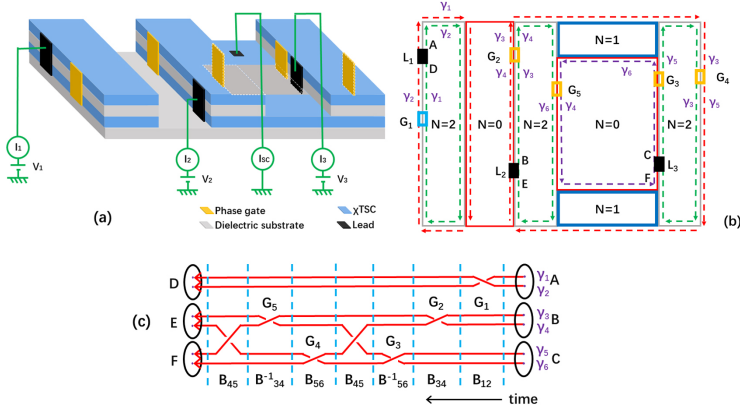


FIG. 4: (Color online) The device for the CNOT. (a) A schematic of a layered χ TSC structure for the CNOT gate. The electric potential of the χ TSC has been set to zero. (b) The top view of (a). G_a , ($a = 1, \dots, 5$) are 5 phase elements. Yellow stickers represent $G(-\frac{\pi}{4})$, and blue one is $G(\frac{\pi}{4})$. (c) The world line of the CNOT.

to a $B_{23}^{(-)}$ gate (Fig. 3(c))

$$B_{23}^{(-)} = \frac{1}{\sqrt{2}} \begin{pmatrix} i & 1 \\ 1 & i \end{pmatrix}. \quad (10)$$

One can also show that $B_{23}^{(+)} = B_{23}^{(-)} \equiv B_{23}$ which is FP-independent. Exchanging γ_1 and γ_2 can be simply realized by adding a phase gate on the upper edge of the double layer thin films in Fig. 3 (d) with $G(\theta) = G(-\frac{\pi}{4})$.

The corresponding phase gates $B_{12}^{(\pm)}$ are also the same, i.e., $B_{12} = \text{diag}(1, i)$, which is the $\frac{\pi}{4}$ -phase gate. The braiding matrix B_{34} , which is realized by adding $G(-\frac{\pi}{4})$ on the lower edge instead of adding it on the upper edge in Fig. 3 (d). However, we find that $B_{34}^{(-)}$ is not the same as $B_{34}^{(+)}$ because $B_{34}^{(+)} = \text{diag}(1, i)$ while $B_{34}^{(-)} = \text{diag}(i, 1)$.

With these basic braiding matrices, we can make the Hadamard gate, up to a global phase i ,

$$B_{12}B_{23}B_{12} \sim H = \frac{1}{\sqrt{2}} \begin{pmatrix} 1 & 1 \\ 1 & -1 \end{pmatrix}. \quad (11)$$

And also $H \sim B_{34}^{(-)}B_{23}B_{34}^{(-)} \sim B_{34}^{(+)}B_{23}B_{34}^{(+)}$ up to a sign. Therefore, the Hadamard gate is also FP-independent when the basis for 1-qubit is properly chosen. Furthermore, we have $Z = B_{12}^2$, $X = HZH$ and $Y = (ZH)^2$. Up to a global phase, they all are independent of the FP. In this way, we have a set of FP-independent Clifford gates.

In general, Fig. 3 (d) gives a phase gate $B(\theta/2) = \text{diag}(1, G(-\theta)) \sim \text{diag}(G(\theta/2), G(-\theta/2))$. The topological phase gates through anyon braiding are $B(-\frac{\pi}{10})$, $B(-\frac{2\pi}{5})$ as well as $B(\frac{\pi}{10}) = B^9(-\frac{\pi}{10}) = B^{-1}(-\frac{\pi}{10})$, and so on. They are independent of the FP of the 1-qubit.

B. The CNOT Gate

To achieve universal TQC, we design a CNOT gate for 2-qubits using six χ MEMs $\gamma_1, \dots, \gamma_6$. The setup of the CNOT gate is FP-dependent. We first take the basis with even total FP as an example, i.e., the incoming basis

$$(|0_A0_B0_C\rangle, |0_A1_B1_C\rangle, |1_A0_B1_C\rangle, |1_A1_B0_C\rangle)^T \quad (12)$$

and the outgoing basis

$$(|0_D0_E0_F\rangle, |0_D1_E1_F\rangle, |1_D0_E1_F\rangle, |1_D1_E0_F\rangle)^T. \quad (13)$$

The device is shown in Fig. 4 (a) and its top view in Fig. 4(b). If we use the elements $G_a(\theta_a)$ with $\theta_1 = \frac{\pi}{4}$ and $\theta_{2,3,4,5} = -\frac{\pi}{4}$, the braiding matrices for 2-qubits are $B_{12}^{(2)} = \text{diag}(1, 1, i, i)$, $B_{34}^{(2)} = \text{diag}(1, i, 1, i)$, and $B_{56}^{(2)} = \text{diag}(1, i, i, 1)$ (See Fig. 4(c)). $B_{45}^{(2)}$ in Fig. 4(c) is the 2-qubits counterpart of the B_{23} gate,

$$B_{45}^{(2)} = \frac{1}{\sqrt{2}} \begin{pmatrix} i & 1 & 0 & 0 \\ 1 & i & 0 & 0 \\ 0 & 0 & i & 1 \\ 0 & 0 & 1 & i \end{pmatrix}$$

where the subscripts stand for the relative positions of the γ_s at a given time slice. According to the sequence of the B -matrices in Fig. 4(c), we obtain the CNOT gate

$$\begin{aligned} \text{CNOT}^{(+)} &= B_{45}^{(2)}B_{34}^{(2)}B_{56}^{(2)}B_{45}^{(2)}B_{56}^{(2)}B_{34}^{(2)}B_{12}^{(2)-1} \\ &= \begin{pmatrix} 1 & 0 & 0 & 0 \\ 0 & 1 & 0 & 0 \\ 0 & 0 & 0 & 1 \\ 0 & 0 & 1 & 0 \end{pmatrix}. \end{aligned} \quad (14)$$

When the input state is chosen as the odd FP 2-qubits, the device in Fig. 4 does not produce the CNOT gate but the matrix

$$i \begin{pmatrix} 0 & 1 & 0 & 0 \\ 1 & 0 & 0 & 0 \\ 0 & 0 & -1 & 0 \\ 0 & 0 & 0 & -1 \end{pmatrix}. \quad (15)$$

The controlling qubit and the target qubit exchange while a sign difference exists. This cannot fulfill the logical task as the CNOT gate. If we input the odd FP 2-qubits, to have the $\text{CNOT}^{(-)}$, the phase gates should be reassigned: We use the elements $G_{1,2,4}(\theta_1) = -\frac{\pi}{4}$ and $G_{3,5}(\theta_{3,5}) = \frac{\pi}{4}$. This gives

$$B_{45}^{(2)}B_{34}^{(2)-1}B_{56}^{(2)}B_{45}^{(2)}B_{56}^{(2)-1}B_{34}^{(2)}B_{12}^{(2)} = \begin{pmatrix} 1 & 0 & 0 & 0 \\ 0 & 1 & 0 & 0 \\ 0 & 0 & 0 & 1 \\ 0 & 0 & 1 & 0 \end{pmatrix}. \quad (16)$$

C. Universal Topological Quantum Gates

The authors of Ref. [78] proved the universality of the quantum circuit models which is equivalent to Ref.

[79]. They chose three gates $\{H, Z^{\frac{1}{4}} = B(\frac{\pi}{8}), \text{CNOT}\}$ as their universal set. In their proof, the key essence is that they can create two orthogonal axes and a phase with irrational number times π from the universal set, namely, any element in $\text{SU}(2)$ can be approximated in a desired precision. Here we will show the existence of the orthogonal axes and the irrational number for strongly correlated Majorana fermion based the TQC.

The universal set that we choose is $\{H, \sqrt{Z} = B(\frac{\pi}{4}), B(-\frac{\pi}{10}), \text{CNOT}\}$. They all have been obtained in last two subsections. Therefore, our universal set is topo-

logical and fault-tolerant. Similar to those in [78], we use

$$X^{\frac{2}{n}} = HB\left(\frac{\pi}{n}\right)H, \quad (17)$$

and define

$$F_{2/5} = X^{2/5}B\left(\frac{\pi}{4}\right)X^{-2/5}, \quad (18)$$

and

$$U_1 = e^{i\lambda\pi\hat{n}_1\cdot\vec{X}} \equiv B\left(-\frac{\pi}{10}\right)X^{\frac{1}{5}} = \frac{1}{8} \begin{pmatrix} 5 + \sqrt{5} + i\sqrt{10 - 2\sqrt{5}} & 3 - \sqrt{5} - i\sqrt{10 - 2\sqrt{5}} \\ -3 + \sqrt{5} - i\sqrt{10 - 2\sqrt{5}} & 5 + \sqrt{5} - i\sqrt{10 - 2\sqrt{5}} \end{pmatrix}, \quad (19)$$

$$U_2 = e^{i\lambda\pi\hat{n}_2\cdot\vec{X}} \equiv F_{2/5}^{-1}U_1F_{2/5} = \frac{1}{32} \begin{pmatrix} (4 + 4i)\sqrt{5} + 20 & (\sqrt{5} - 1)(8i + \sqrt{10 - 2\sqrt{5}}) \\ -(\sqrt{5} - 1)(-8i + \sqrt{10 - 2\sqrt{5}}) & (4 - 4i)\sqrt{5} + 20 \end{pmatrix}, \quad (20)$$

where $\vec{X} = (X, Y, Z)$; λ_i and unit vectors \hat{n}_i are to be determined. Thus, solving Eqs. (19) and (20), we find that $\lambda_1 = \lambda_2 = \lambda$ where λ is given by

$$\cos(\lambda\pi) = \cos^2 \frac{\pi}{10} = \frac{5 + \sqrt{5}}{8}, \quad (21)$$

while

$$\begin{aligned} \hat{n}_1 &\approx (-0.293893, 0.0954915, 0.293893), \\ \hat{n}_2 &\approx (0.309017, 0.0908178, 0.279508). \end{aligned}$$

Clearly, $\hat{n}_1 \cdot \hat{n}_2 = 0$. Furthermore, $e^{i2\lambda\pi}$ is the non-cyclotomic root of the irreducible monic polynomial equation $x^4 + x^3/4 + x^2/16 + x/4 + 1 = 0$. Hence, λ is irrational. If constructing a local isomorphism from $\text{SU}(2)$ to $\text{SO}(3)$, then any element of $\text{SU}(2)$ can be expressed as an Euler rotation. That is, if α, β and γ are the Euler angles, any elements of $\text{SU}(2)$ can be written as [87] $e^{i\phi\hat{n}\cdot\vec{X}} = e^{i\alpha\hat{n}_1\cdot\vec{X}}e^{i\beta\hat{n}_2\cdot\vec{X}}e^{i\gamma\hat{n}_1\cdot\vec{X}}$. Because λ is irrational, there are a, b and c such that $\alpha \approx a\lambda\pi, \beta \approx b\lambda\pi$ and $\gamma \approx c\lambda\pi$, i.e.,

$$e^{i\phi\hat{n}\cdot\vec{X}} \approx (U_1)^a(U_2)^b(U_1)^c, \quad (22)$$

where a, b and c are integers determined by α, β , and γ in a desired precision. This gives the proof of the universality of $\{H, \sqrt{Z} = B(\frac{\pi}{4}), B(-\frac{\pi}{10}), \text{CNOT}\}$ according to [79].

VI. ELECTRIC SIGNALS OF THE OUTPUTS

Since the initial and final states are the charged fermions, the inputs and readout of the designed TQC

are electric. To read out the computation results of the TQC, we must translate the outgoing states of the quantum gate operations into electric signals.

For the ZH gate, the conductance between the leads at the two ends of the device measures the operating result [65]. For the other 1-qubit gates, the conductance calculation is also direct. Here, we give an example for the 2-qubits, the CNOT gate. The incoming and outgoing bases are given by (12) and (13), respectively. The FP 0 or 1 can be read out by the electric signals at the leads. The CNOT gate changes $|1_A0_B1_C\rangle$ to $|1_A1_B0_C\rangle$ and vice versa, while keeping $|0_A0_B0_C\rangle$ and $|0_A1_B1_C\rangle$ unchanged. Thus, these states changes can be read out from the conductance between Lead 2 and Lead 3: $\sigma_{23} = (1 - \langle\psi_{out}|\psi_{in}\rangle)\frac{e^2}{h}$. Namely, $\sigma_{23} = e^2/h$ for $|\psi_{in}\rangle = |1_A0_B1_C\rangle$ or $|1_A1_B0_C\rangle$ while $\sigma_{23} = 0$ for $|\psi_{in}\rangle = |0_A0_B0_C\rangle$ or $|0_A1_B1_C\rangle$.

If the phases in $G_a(\theta_a)$ in Fig. 4 are arbitrary, the outgoing state $|\psi_{out}\rangle$ is given by $|\psi_{out}\rangle = U(\theta_a)|\psi_{in}\rangle$ where $|\psi_{in}\rangle$ is the incoming state and $U(\theta_a)$ is the unitary transformation (See Appendix E). For example, for an incoming state $|\psi_{in}\rangle = |0_A0_B0_C\rangle$, the outgoing state is $|\psi_f\rangle = -\frac{1}{2}(1 - e^{-i\theta_5})|0_A0_B0_C\rangle + \frac{1}{2}[ie^{-i\theta_{12}}(1 + e^{-i\theta_5})]|0_A1_B1_C\rangle$ and the corresponding conductance is $\sigma_{23} = \cos^2(\theta_5)\frac{e^2}{h}$. For the topological CNOT gate, these $G_a(\theta_a)$ are given by the device in $\theta_2 = \theta_3 = \theta_4 = \theta_5 = -\frac{\pi}{4}$ and $\theta_1 = \frac{\pi}{4}$, and σ_{23} exactly gives the result we analyzed before.

Before ending this section, we would like to discuss the spin polarization problem. We assume the $p_x + ip_y$ χ TSC is a spinless fermion system. In reality, it should be a spin polarized system. First we would like to emphasize that a calculating unit, i.e., the quantum circuit, must be in connection to one bulk of TSC in order to prevent the phase loss of the phase gates. Therefore, the spin of the

Cooper pairs in the circuit is all of the same polarization and so the spin of the chiral edge states is. A real spin polarized χ TSC material is not yet ready in nature. If it was found, the Cooper pair's spin would be fixed by the materials. The electron's spin from Leads to the edge of TSC will be automatically selected by the TSC. A better choice is using spin selecting valve, e.g., injecting in and putting out the electrons from a ferromagnet [82], anomalous Rashba metal/superconductor junctions [83] or in noncollinear antiferromagnets [84], in order to prevent the opposing spin electrons affect the data read in and out. In these cases, a gap opens between the spin majority electron and spin minority electron near the Fermi level. The conversion losses mainly depend on the mismatch of Fermi velocities, the polarizability, and the energy of electronics. Lower mismatch of Fermi velocities and higher polarizability are expected to get fewer losses.

VII. THE QUANTUM CIRCUITS WITH TOPOLOGICAL QUANTUM GATES

We have constructed a set of universal quantum gates for 1-qubit and the CNOT gate. In principle, we can use them to construct the quantum circuit models associated with quantum algorithms, e.g., the quantum Fourier transformation, a classical adder with quantum gates, and then Shor's integer factorization algorithm. However, the conventional TQC process with non-Abelian anyon does not follow the quantum circuit models. In the former, a larger qubit gate is not simply constructed by the smaller gates. Our CNOT gate construction is an example because it is not assembled by two 1-qubit gates. In fact, an n -gate in this quantum computation uses $2n + 2$ MEMs (Fig. 5 (a)). This is called the 'dense encoding' process [80]. With the quantum circuit model, an n -gate is constructed by $4n$ MEMs (Fig. 5 (b)). This process matches with the quantum circuit model and is called the 'sparse encoding' process [80]. In order to encode Shor's algorithm, we take the sparse encoding. Since the set of universal quantum gates for the 1-qubit is not dependent on the FP of the 1-qubit, they are good elements for the quantum circuit. However, in the sparse encoding, one can only prepare qubits in superposition states, but no entanglement states with braiding only [81]. For instance, we cannot make the CNOT gate with two gates for 1-qubit. It has to be realized in the dense encoding as we have shown. Therefore, our process in fact is a mixed one of the sparse-dense encoding. We use six MEMs to construct a CNOT gate. This does not match the quantum circuit model. On the other hand, the CNOT gate we constructed in Sec. V B is dependent on the FP of the 2-qubits. To measure the FP of the 2-qubits, two additional ancillary MEMs are required. This makes a CNOT gate with eight MEMs in the sparse encoding. Adding this sparse encoding CNOT gate to the universal gates for 1-qubit, we can make a quantum

circuit as usual.

To illustrate such a process, we show the quantum circuit with our TQC process for Shor's integer factorization algorithm.

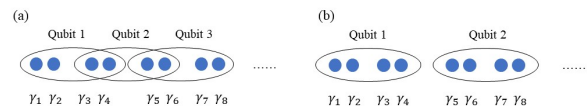


FIG. 5: (Color online) Two different encodings [80].(a) The dense encoding process using $2n + 2$ MEMs to encode n -qubits;(b) The sparse encoding, n -qubits are encoded by $4n$ MEMs.

A. The CNOT Gate in Sparse Encoding

We construct the CNOT gate in the sparse encoding. As we mentioned, two ancillary MEMs will be introduced to measure the FP of the 2-qubits. Notice that the measurements here do not measure the fermion occupation number of the computational states directly, but measure the parity operator $\hat{P} = i\gamma_1\gamma_2\dots$ which won't destroy the coherence of the quantum state. In experiment, we make a side measurement to the total charge or the total spin for the subsystem to determine the eigenvalue of \hat{P} [86].

More specifically, we want to measure the FP of 2-qubits that are input into a CNOT⁽⁺⁾ given by Eq. (14). In the sparse encoding, 2-qubits are associated with 4 pairs MEMs $\gamma_1, \gamma_2, \dots, \gamma_8$, we use the same process taken in Ref. [80], i.e., we enforce $\gamma_1\gamma_2\gamma_3\gamma_4 = \gamma_5\gamma_6\gamma_7\gamma_8 = +1$ (or -1). We take $\gamma_{4,5}$ as an ancillary qubit and measure its FP, i.e., $i\gamma_4\gamma_5$ (Fig. 6). Thus, γ_6 exchanges with $\gamma_{4,5}$ and forms a new pair with γ_3 .

If $i\gamma_4\gamma_5 = 1$ (or -1), the remaining six MEMs form 2-qubits in the dense encoding with even FP. We then use the 2-qubits as the input state to a CNOT⁽⁺⁾ given by Eq. (14), according to the selected parity of the CNOT⁽⁺⁾ (See Fig. 6). Otherwise, we do the measurement again until $i\gamma_4\gamma_5 = 1$ (or -1). Finally, we add $\gamma_{4,5}$ back and exchange γ_6 with $\gamma_{4,5}$ again, then measure $\gamma_5\gamma_6\gamma_7\gamma_8$. If it is 1 (or -1), the eight MEMs return to a 2-qubits with the positive FP in the sparse encoding which is the output state (Fig. 6). In this way, we encode the CNOT gate with the sparse encoding. For more details, see Appendix F.

We can improve the efficiency in inputting. After making the measurement M_1 , we can switch θ_1 from $-\frac{\pi}{4}$ to $\frac{\pi}{4}$ and $\theta_{3,5}$ from $-\frac{\pi}{4}$ to $\frac{\pi}{4}$ if $i\gamma_4\gamma_5 = -1$ (or 1) as we will see in Sec. VIII. In this case, the CNOT⁽⁺⁾ gate becomes the CNOT⁽⁻⁾. Thus, instead of abandoning the FP negative state, it can be used. We next add back $\gamma_{4,5}$ and do the similar operations to return the 2-qubits in the sparse encoding as before. Furthermore, we can further improve the efficiency if the FP measurement in M_2 is wrong by correcting FP, which will not be studied here.

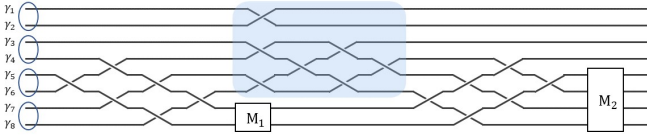


FIG. 6: (Color online) The CNOT in sparse encoding with even parity. The blue shade area is the same as the dense encoding CNOT⁽⁺⁾ (Fig. 4 (c)). Because of the no-entanglement rule, two FP measurements are needed to get the entanglement states.

B. Brief Introduction of Shor's Algorithm

In the coming several subsections, we describe Shor's integer factorization algorithm with our TQC process. We first give a brief introduction to Shor's algorithm [88].

The key step of Shor's algorithm is turning the integer factorization problem to a period-finding problem and then uses quantum computer to realize a period-finding subroutine, i.e., to find the period r of the function $f(x) = a^x \bmod N$, where N is the integer waiting to be factorized and a is an arbitrary number that is coprime with N . Calculating the greatest common divisors $n_1 = \gcd(a^{\frac{r}{2}+1}, N)$ and $n_2 = \gcd(a^{\frac{r}{2}-1}, N)$, then $N = n_1 \cdot n_2$, which can be realized by Euclid's algorithm classically.

We denote the basis of a 1-qubit with a given FP, e.g., $\{|0^{\gamma_1 \gamma_2 1^{\gamma_3 \gamma_4}}, |1^{\gamma_1 \gamma_2 0^{\gamma_3 \gamma_4}\rangle\}$ as $\{|0\rangle, |1\rangle\}$. Starting from two registers in which Register 1 = $|0^l\rangle$ which is the product of l $|0\rangle$ and Register 2 = $|0^q\rangle$. The quantum part of Shor's algorithm, the period-finding subroutine, is composed by three steps [88]: (i) Doing the quantum Fourier transformation to Register 1 with $2^q = N$, $n = 2^l$ is a number within $(N^2, 2N^2)$

$$|0^l\rangle|0^q\rangle \rightarrow (F_n|0^l\rangle)|0^q\rangle = \frac{1}{\sqrt{n}} \sum_{x=0}^{n-1} |x\rangle|0^q\rangle \quad (23)$$

where $|x\rangle$, e.g., $|0\rangle = |0\dots 0\rangle$, $|1\rangle = |0\dots 01\rangle$, $|2\rangle = |0\dots 011\rangle$, etc., label the basis vectors of l -qubits. That is, the basis vector $|x\rangle$ indicates a binary number corresponding to x .

(ii) Doing the modular exponentiation U_f such that

$$U_f \frac{1}{\sqrt{n}} \sum_{x=0}^{n-1} |x\rangle|0^q\rangle = \frac{1}{\sqrt{n}} \sum_{x=0}^{n-1} |x\rangle|f(x)\rangle \quad (24)$$

Making a measurement on Register 2 such that the state in Register 1 collapses to

$$\frac{1}{\sqrt{m}} \sum_{j=0}^{m-1} |jr + s\rangle$$

where s is some number less than r and m is the number of $f(x) = f(s)$ with $x \in \{0, \dots, n-1\}$.

(iii) Doing the quantum Fourier transformation again

to Register 1 and measuring

$$F_n \frac{1}{\sqrt{m}} \sum_{j=0}^{m-1} |jr + s\rangle,$$

we obtain a random number y . Repeat the process again, we have a new y . The maximal one in a series of y is the period r .

Fig. 7 is the schematic of Shor's period-finding algorithm. In the following we explain the detailed algorithms for the quantum Fourier transformation and the modular exponentiation with our quantum circuit model.

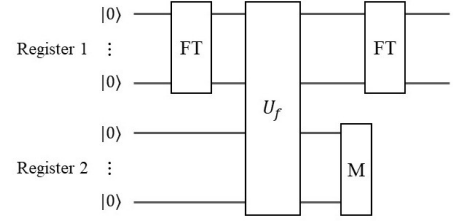


FIG. 7: The period-finding subroutine. It is composed by three steps: Do the quantum Fourier transformation (FT) to Register 1; apply the modular exponentiation U_f and measure Register 2 such that the state in Register 1 collapses. Do the quantum Fourier transformation to Register 1 again. Finally, measure the output state in Register 1.

C. Quantum Fourier Transformation

Quantum Fourier transformation is the quantum analogue of the discrete Fourier transformation, which plays an important role in many quantum algorithms [88]. The circuit implementation is shown in Fig. 8. It consists of the Hadamard gate and the controlled-phase gate *controlled* - B_n with $B_n = B(-\frac{\pi}{2^n})$.

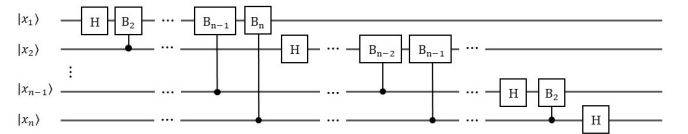


FIG. 8: The circuit implementation for quantum Fourier transformation.

The controlled-phase gate is a two-qubit gate, i.e., the target qubit is acted by a phase gate,

$$\text{controlled} - B_n = \begin{pmatrix} 1 & 0 & 0 & 0 \\ 0 & 1 & 0 & 0 \\ 0 & 0 & e^{-i\pi/2^n} & 0 \\ 0 & 0 & 0 & e^{i\pi/2^n} \end{pmatrix} \quad (25)$$

Controlled-gates are a kind of gates often used in quantum computation and are proven to be decomposed into

the combination of CNOT and 1-qubit gates [79]. In case of the controlled- B_n , one of the decomposition methods is given by Fig. 9, i.e., the controlled- B_n is composed by the 1-qubit gate B_{n+1} ,

$$B_{n+1} = \begin{pmatrix} e^{-i\pi/2^{n+1}} & 0 \\ 0 & e^{i\pi/2^{n+1}} \end{pmatrix} \quad (26)$$

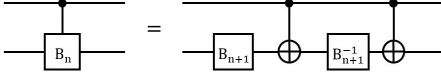


FIG. 9: The decomposition of the controlled- B_n .

We see that B_{n+1} is a group element of $SU(2)$. For example, for the controlled- B_2 gate (B_2 is often called the S gate or $\frac{\pi}{4}$ -gate), $B(\frac{\pi}{8})$ (also called the $\frac{\pi}{8}$ -phase gate or T -gate) is needed. As we have shown, it can be approximated by Eq. (22). When $a = 18, b = 22$ and $c = 17$, Eq. (22) gives the T -gate in a precision $> 97\%$.

Any 1-qubit quantum gate can be approximated by Eq. (22) and a rough calculation can estimate the circuit scale. Suppose a quantum gate within the accuracy range σ is needed. This is equivalent to move a vector \mathbf{A} on a Bloch sphere to a designated point by rotating about two orthogonal axes $M = a + b + c$ times successively. M operations will give a total of $\frac{1}{6}(M+1)(M+2)(M+3)$ different points on the Bloch sphere. It requires that these points can cover the sphere. Defining the accuracy requirement as the solid angle range of the vector neighborhood, then $\frac{1}{6}(M+1)(M+2)(M+3) \cdot \sigma \sim 4\pi$. With the accuracy requirement σ , it takes about $M \sim \sqrt[3]{\frac{24\pi}{\sigma}}$ steps to get the desired quantum gate. This argument, however, doesn't depend on the specific gate, but only related to the accuracy, is an estimate of the upper limit. For some special gate, much less operations are required.

D. Adder and Toffoli Gate

As we have seen, the modular exponentiation applies following transformation

$$U_f |x\rangle \otimes |0^q\rangle \rightarrow |x\rangle \otimes |a^x \bmod N\rangle,$$

where $|x\rangle$ and $|0^q\rangle$ represent two registers and the U_f is determined by a and N . The elementary block for a computer to realize basic arithmetic operations is the addition unit or called an adder. Starting from the adder, Vedral et al. provide an explicit construction of quantum circuit to realize modular exponentiation [89]. A plain adder is constructed in Fig. 10, which consists of the CNOT gates and the Toffoli gates.

The Toffoli gate is controlled-controlled-NOT and can be decomposed as

$$\text{Toffoli} = \text{CCX} = H_3 \cdot \text{CCZ} \cdot H_3.$$

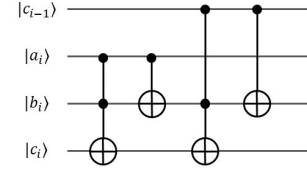


FIG. 10: The construction of adder. $|a_i\rangle$ and $|b_i\rangle$ are the i th qubit of Register 1 and Register 2, respectively. $|c_i\rangle$ represents the i th qubit of the ancillary register to carry the calculation.

Fig. 11 shows one of constructions for the Toffoli gate, where $\text{CCZ} = \text{diag}(1, 1, 1, 1, 1, 1, 1, -1)$ and $H_3 = H \otimes H \otimes H$ with the Hadamard gate acting on the different 1-qubit.

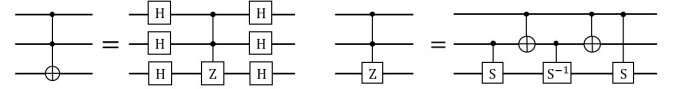


FIG. 11: The constructions for Toffoli gate and CCZ .

We draw the complete logical circuit for Toffoli gate in Fig. 12 (a). And then Fig. 12 (b) gives the braiding diagram with MEMs for the Toffoli gate. Notice that some quantum gates may act on two qubits which are not neighboring but jumping is not allowed in the TQC. One has to move them together first. The operator \hat{U}_1 and \hat{U}_2 are composed by the Hadamard gate and different phase gates (see Section VC). Fig. 12(d) shows the braiding diagram for \hat{U}_1 as an example.

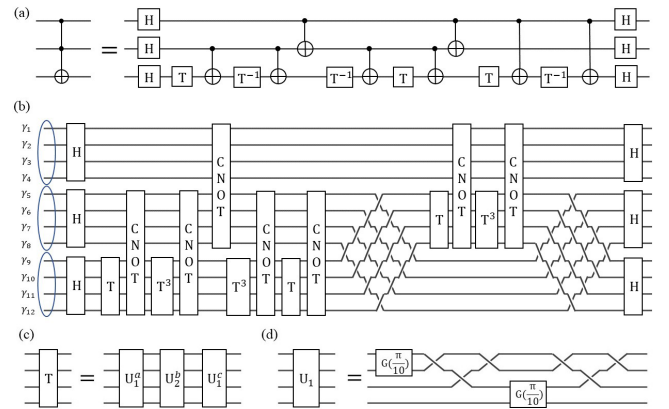


FIG. 12: (a) The complete logical circuit for Toffoli gate. (b) The braiding diagram of (a). (c) The braiding diagram of the T -gate. (d) \hat{U}_1 operator. \hat{U}_2 can be constructed similarly.

VIII. PHYSICAL REALIZATION OF THE QUANTUM CIRCUITS

A. Hadamard Gate

Figs. 3 (a,b,d) and 4 (a,b) are the schematics of the devices for 1-qubit and 2-qubits. Logically, these designed devices are equivalent to their corresponding world line graphs, i.e., Figs. 3 (d) and 4 (c). If we only measure these 1- or 2- qubits, we can use these devices. However, the devices designed in those schematics cannot be used as parts in the quantum circuit because the two-dimensional projects of the devices are topologically different from the world line graphs, which is easy to see by comparing Fig. 3 (b) with (c), and Fig. 4 (b) with (c). Therefore, we change the designation of the devices in three dimensions such that they are adaptive with the world line graphs and then can be used to assemble the quantum circuit.

We first deform Fig. 3 (a) for B_{23} to Fig. 13 (a) where the blue layer is the χ TSC and the gray layer is dielectric substrate as before. The second and the third χ TSC layers are connected by a vertical χ TSC slide and are corresponding to the $N = 1$ base layer in Fig. 3 (a). The top and down layers are corresponding to the two top layers on the right and left hand sides in Fig. 3 (a). The MEMs will run along the edges of χ TSC and we see the braiding between $\gamma_{2,3}$. Fig. 13 (b) are right view of (a). The front view of Fig. 13 (a) maps out the world line (Fig. 13). The matrix B_{23} in (10) is not equal to its inverse. The inverse B_{23}^{-1} is shown in Fig. 13 (d). Its right and front views (Figs. 13 (e) and (f)) indeed show that is an inverse operation.

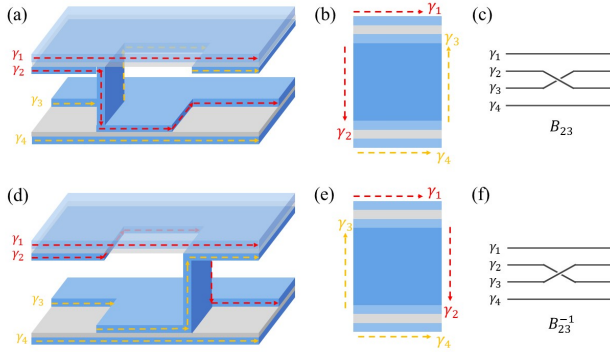


FIG. 13: (Color online) (a)-(c) Device schematic of B_{23} (as well as $B_{2n,2n+1}$). (d)-(f) Device schematic of B_{23}^{-1} . The blue layer is the χ TSC thin films and gray layer is dielectric substrate. To be more intuitive, we make the upper layers translucent. The MEMs runs along the arrows in the edges of thin films.

It is also possible to exchange γ_2 and γ_4 . However, for a 1-qubit gate, the probability of such an exchange is negligible because the low-energy pairing between two incoming fermions is forbidden by the superconducting

gap.

With the basic elements, the Hadamard gate can be constructed as Fig. 14. The yellow stickers are the phase gates.

B. CNOT Gate

Fig. 15 shows the CNOT gate in the dense encoding and will be encapsulated together with two parity measurements corresponding to a logical CNOT gate as Fig. 6. In practical computation processes, if the whole circuit owns n CNOT gates, we only keep the result that $\hat{P}_1 = \hat{P}_2 = \dots = \hat{P}_{2n} = 1$ (or -1 , depending on the selected FP). The probability of getting the useful results is $\frac{1}{4^{2n}}$. However, the speed that a quantum state runs is Fermi velocity v_F which is $\sim 10^{-3}c$. If the device size is in the order of microns, we can input 10^{11} quantum states per second.

As we mentioned in Sec. VII A, we can alternatively choose to switch the $\text{CNOT}^{(+)}$ to the $\text{CNOT}^{(-)}$ after we get $i\gamma_4\gamma_5 = -1$ in M_1 . The probability may increase to $\frac{1}{2^{2n}}$. It is more efficient. The switching between $G(\pm\frac{\pi}{4})$ and $G(\mp\frac{\pi}{4})$ is operable because $G(\frac{\pi}{4}) = G(-\frac{\pi}{4})G(-\frac{\pi}{4})G(-\frac{\pi}{4})$. The switching can be done by connecting either one $G(-\frac{\pi}{4})$ or three $G(-\frac{\pi}{4})$ after receiving the message in terms of M_1 .

To further raise the inputting efficiency is possible instead of abandoning the wrong FP state measured in M_2 . Some different process for measurement-based CNOT are proposed [90]. Instead of abandoning useless messages, they correct the quantum state according to the side measurements. The cost is 6 pairs of MEMs are needed and 2 pairs of them are used to be ancillary and three side measurements are made. We can also realize this kind of measurement-based CNOT by the topological superconductor thin films. The advantage is the inputting efficient may greatly lift. How to correct the abandoning message in our algorithm is not studied here.

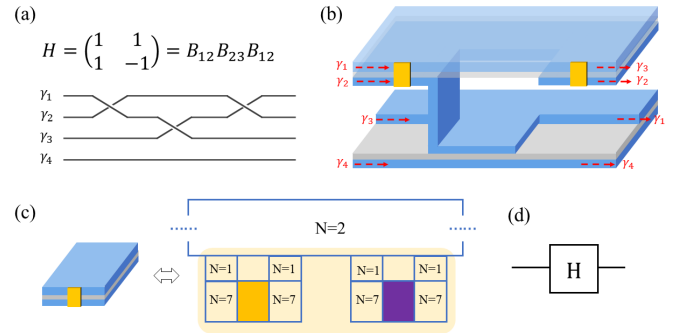


FIG. 14: (Color online) The construction of Hadamard gate. (a) The world line. (b) The device schematic. The yellow stickers are the phase gates. (c) The phase gate revisits. The yellow sticker on the left-hand side corresponds to the yellow shade area on the right-hand side, which is equivalent to Fig. 2 (a) (d). The Hadamard gate in the quantum circuit model.

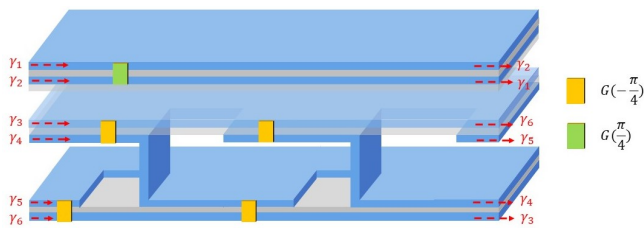


FIG. 15: (Color online) Braiding device of the CNOT in the dense encoding, corresponding to the blue box in Fig. 6. The green stickers are the $-\pi/4$ phase gates and the yellow ones are the inverse of the $\pi/4$ gates. It will be encapsulated together with two parity measurements corresponding to a logical CNOT gate in the sparse encoding.

IX. CONCLUSIONS

We proposed a new route to design a universal TQC. We showed that the universal TQC based on strongly corrected MEMs coincides with the conventional quantum circuit models. We have noticed that some quantum gates we designed are dependent on the FP of the input qubits. To construct the multi-qubits and the corresponding unitary transformation by braiding, we have used the sparse-dense mixed encoding process which is based on the FP side measurement to the ancillary qubits. We discussed the possibility to raise the inputting efficiency. We constructed a quantum circuit model for Shor's algorithm with our devices. In general, our process can be applied to all existed and new quantum algorithms in study [91]. Without the FP measurement, we should follow the unitary category approach developed for the TQC [20]. In this work, we do not do a full dense encoding construction for a universal TQC with our devices, which is a next task. We here take the strong coupling limit in which τ are reflected while the ε are transmitted by interacting barrier. In reality, the reflection of anyons is not complete, but of a statistical correction as a recent experiment showed [76]. We will leave this effect from the anyon collisions to the TQC in a further study. We showed that some quantum operating results can transfer to the electrical signs of the output states, e.g., the CNOT gate's in the dense encoding as well as the 1-qubit's. However, for a quantum circuit, because we take the sparse encoding and there are the other complex conditions, we do not discuss its electric sign of the output. We will also study these issues in future.

Acknowledgements

The authors thank Y. S. Wu for valuable discussions. This work is supported by NNSF of China with No. 12174067 (YMZ, BC,YY,XL), No. 11474061 (YMZ,YGC,YY,XL) and No. 11804223 (BC,XL) and the U.S. Department of Energy, Basic Energy Sciences

Grant No. DE-FG02-99ER45747 (ZW).

Appendix A: Non-Abelian statistics of Majorana fermion approaches

We explain when the Majorana fermions are Abelian and when they are non-Abelian.

1. One Species of Majorana Fermions

Consider N -Majorana fermions which are of the same species, say, $\gamma(x_i)$, $i = 1, \dots, N$, as in the $\nu = 5/2$ FQHE and the Ising model [24]. Let us begin with the following Majorana fermion relations

$$\begin{aligned}\gamma(x_i)\gamma(x_j) &= -\gamma(x_j)\gamma(x_i), \text{ if } x_i \neq x_j \\ \gamma(x_i)\gamma(x_j) &= 1, \text{ if } x_i = x_j.\end{aligned}$$

The quantum states at a given spatial point x are $|\psi_+\rangle \oplus |\psi_-\rangle$ where $|\psi_\pm\rangle$ have fermion parity \pm . The fermion parity means whether the number of Majorana fermions is even or odd. The fusion rules are $\psi_+\psi_+ = \psi_+$, $\psi_+\psi_- = \psi_-$, $\psi_-\psi_- = \psi_+$, i.e., one species of many Majorana fermions are Abelian.

To enable non-Abelian statistics, one needs to introduce other degrees of freedom, e.g., vortices. If there is a vortex excitation besides the Majorana fermions at a given x , i.e., a Majorana bound state, we have the basis

$$(|\psi_{+,0}\rangle, |\psi_{-,0}\rangle, |\psi_{+,1}\rangle, |\psi_{-,1}\rangle) \cong (I, \psi, \sigma, \sigma \times \psi = \mu). \quad (\text{A1})$$

where $|\psi_{p,a}\rangle$ are the states with the fermion parity $p = \pm$ and the vortex number 0, 1. The right hand side of \cong is the primary fields in the Ising model. According to the Ising model, the non-Abelian anyon is the Majorana bound state, 1 qubit, $\tilde{\sigma} = (\sigma + \mu, \sigma - \mu)$ which has the non-Abelian fusion rule $\tilde{\sigma} \times \tilde{\sigma} = I + \psi$.

With anyon $\tilde{\sigma}$, one can construct the quantum gates $\{H, \sqrt{Z}, CNOT\}$ and then TQC can be partially encoded.

2. Two Species of Majorana Fermions

Now, let us discuss two species of Majorana fermions, which is the case in the main text, where a spinless (or spin polarized) conventional fermion Ψ can be decomposed into two species of Majorana fermions $\Psi(x_i) = \frac{1}{\sqrt{2}}(\gamma^{(1)}(x_i) + i\gamma^{(2)}(x_i))$. Ψ 's anti-communication relations

$$\{\Psi(x_i), \Psi(x_j)\} = 0, \{\Psi(x_i), \Psi^\dagger(x_j)\} = \delta_{ij}$$

require

$$\begin{aligned}\gamma^{(1)}(x_i)\gamma^{(2)}(x_j) &= -\gamma^{(1)}(x_j)\gamma^{(2)}(x_i), \text{ for any } x_i \text{ and } x_j \\ \gamma^{(a)}(x_i)\gamma^{(a)}(x_j) &= -\gamma^{(a)}(x_j)\gamma^{(a)}(x_i), \text{ for } x_i \neq x_j \\ \gamma^{(a)}(x_i)\gamma^{(a)}(x_j) &= 1, \text{ for } x_i = x_j\end{aligned}$$

Notice that two species of Majorana fermions are necessary to form a conventional (charged) fermion. If $\gamma^{(1)} \equiv \gamma^{(2)}$, i.e., they were the same species Majorana fermion, one could not obtain the above commutators for the conventional fermion.

For the conventional fermion in the normal states, the the particle number is conserved. The single particle state is $|\phi_n\rangle$ for the particle number $n = 0, 1$. We have the the well-known Fermi statistics which is Abelian.

In a superconductor, the single particle number is no longer a conserved quantity as a pair of electrons can turn into a Cooper pair and vice versa. However, the fermion parity, i.e., the odd/even number of the single particles, is conserved since the single particles are created or annihilated in pairs. Furthermore, in the edges of multi-layer thin films of a topological superconductor, two Majorana fermions from the injected conventional fermion can be delocalized to the edges of the different films (similar to two delocalized Majorana zero modes at the two ends of a Kitaev chain). Thus, the quantum states at a position x along the edge form the basis

$$(|\varphi_{+,+}\rangle, |\varphi_{-,-}\rangle) \oplus (|\varphi_{+,-}\rangle, |\varphi_{-,+}\rangle) \equiv \Phi_e \oplus \Phi_o, \quad (\text{A2})$$

where the subscripts $a, b = \pm$ in $\psi_{a,b}$ refer to the fermion parity of the first and second species of Majorana fermion. $\Phi_{e,o}$ refers to the sector with the total fermion parity even/odd. Each sector with a given total fermion parity is two-fold degenerate. The fusion rule is $\Psi_o \times \Psi_o = \varphi_{+,+} + \varphi_{-,-}$. Then being isomorphic to the Ising primary fields, $\Psi_e \cong (I, \psi)$ while $\Psi_o \cong (\sigma, \mu) \cong \tilde{\sigma}$, which is the 1-qubit. Thus, we recover the fusion rule as that in the Ising model. Hence, the many-body Majorana fermions of two species at the edge of multilayer thin films of the topological superconductor obey non-Abelian statistics.

This is also the case for the Kitaev chain [31], the gapless Majorana edge modes of Kitaev honeycomb spin model [19], and the model of Lian et al. [65].

This two species approach has in fact been studied in earlier pioneering works, e.g., Nayak and Wilczek (Section 9 in [32]) and Ivanov [33].

As we showed in this work, since we cannot braid the two Majorana objects from a charged fermion, we do not have \sqrt{Z} gate. Thus, this type of non-Abelian Majorana

objects cannot be used to design a TQC because there is no a topological CNOT in this scheme.

Appendix B: Basic facts of G_2

Although Hu and Kane listed most of the useful contents of G_2 in their work [1], we would like to concisely repeat part of them for reader's convenience. The simplest exceptional Lie group G_2 as a subgroup of $SO(7)$ keeps $\sum_{a,b,c=1}^7 \hat{f}_{abc} \gamma_a \gamma_b \gamma_c$ invariant. We choose the nonzero total antisymmetric \hat{f}_{abc} to be [92]

$$\hat{f}_{124} = \hat{f}_{235} = \hat{f}_{346} = \hat{f}_{457} = \hat{f}_{561} = \hat{f}_{672} = \hat{f}_{713} = 1, \quad (\text{B1})$$

and the permutations. The 21 generators of $SO(7)$ can be represented by 7×7 skew matrices $L_{ab}^{m,n} = i(\delta_{ma}\delta_{nb} - \delta_{na}\delta_{mb})$ where $m < n = 1, \dots, 7$. The dimensions of G_2 is 14 and the generators Ξ^α of the fundamental representation of G_2 is given by [1, 93]

$$\Xi^\alpha = \begin{cases} \frac{L^{\alpha,\alpha+2} - L^{\alpha+1,\alpha+5}}{\sqrt{2}}, & \alpha = 1, \dots, 7 \\ \frac{L^{\alpha,\alpha+2} + L^{\alpha+1,\alpha+5} - 2L^{\alpha+3,\alpha+4}}{\sqrt{6}}, & \alpha = 8, \dots, 14. \end{cases} \quad (\text{B2})$$

The quadratic Casimir operator is given by

$$\sum_{\alpha=1}^{14} \Xi_{ab}^\alpha \Xi_{cd}^\alpha = \frac{2}{3}(\delta_{ad}\delta_{bc} - \delta_{ac}\delta_{bd}) - \frac{1}{18} \sum_{efg} \epsilon_{abcdefg} \hat{f}_{efg}, \quad (\text{B3})$$

where $\epsilon_{abcdefg}$ is the 7-dimensional total antisymmetric tensor.

Appendix C: Details of the interaction terms

The interactions in the main text read

$$H_i = -\frac{\lambda}{3} \sum_{a \neq b} \gamma_a^R \gamma_b^R \gamma_b^L \gamma_a^L - \frac{\lambda}{3} \sum' \gamma_a^R \gamma_b^R \gamma_c^L \gamma_d^L, \quad (\text{C1})$$

where \sum' means the summation runs the indices with $\epsilon_{abcdefg} \hat{f}_{efg} = -1$. In Fig. 16, we give an example of the interaction domains, i.e., $\gamma_3^L \gamma_5^L \gamma_6^R \gamma_7^R$. There are 42 terms in the first sum of Eq. C1 and half of them are non-equivalent. There are also 42 terms in the second sum. We list all of them as follows:

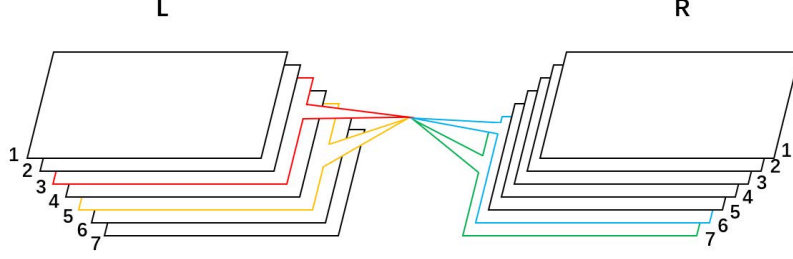


FIG. 16: (Color online) The illustrations of the interactions $\gamma_3^L \gamma_5^L \gamma_6^R \gamma_7^R$. Each layer provides a χ MEM channel with Chern number $N = 1$. The detailed illustrations at the joint of Layer 3L, 5L, 6R, and 7R are shown in Fig. 1(b) and (d) in the main text.

$$\begin{aligned} \sum_{a \neq b} \gamma_a^R \gamma_b^R \gamma_b^L \gamma_a^L &= 2 \sum_{a < b} \gamma_a^R \gamma_b^R \gamma_b^L \gamma_a^L \\ &= 2(\gamma_1^R \gamma_2^R \gamma_2^L \gamma_1^L + \gamma_1^R \gamma_3^R \gamma_3^L \gamma_1^L + \gamma_1^R \gamma_4^R \gamma_4^L \gamma_1^L + \gamma_1^R \gamma_5^R \gamma_5^L \gamma_1^L + \gamma_1^R \gamma_6^R \gamma_6^L \gamma_1^L + \gamma_1^R \gamma_7^R \gamma_7^L \gamma_1^L + \gamma_2^R \gamma_3^R \gamma_3^L \gamma_2^L \\ &+ \gamma_2^R \gamma_4^R \gamma_4^L \gamma_2^L + \gamma_2^R \gamma_5^R \gamma_5^L \gamma_2^L + \gamma_2^R \gamma_6^R \gamma_6^L \gamma_2^L + \gamma_2^R \gamma_7^R \gamma_7^L \gamma_2^L + \gamma_3^R \gamma_4^R \gamma_4^L \gamma_3^L + \gamma_3^R \gamma_5^R \gamma_5^L \gamma_3^L + \gamma_3^R \gamma_6^R \gamma_6^L \gamma_3^L \\ &+ \gamma_3^R \gamma_7^R \gamma_7^L \gamma_3^L + \gamma_4^R \gamma_5^R \gamma_5^L \gamma_4^L + \gamma_4^R \gamma_6^R \gamma_6^L \gamma_4^L + \gamma_4^R \gamma_7^R \gamma_7^L \gamma_4^L + \gamma_5^R \gamma_6^R \gamma_6^L \gamma_5^L + \gamma_5^R \gamma_7^R \gamma_7^L \gamma_5^L + \gamma_6^R \gamma_7^R \gamma_7^L \gamma_6^L), \end{aligned} \quad (C2)$$

$$\begin{aligned} \sum_a' \gamma_a^R \gamma_b^R \gamma_c^L \gamma_d^L &= \gamma_3^R \gamma_5^R \gamma_6^L \gamma_7^L + \gamma_3^R \gamma_6^R \gamma_5^L \gamma_7^L + \gamma_3^R \gamma_7^R \gamma_5^L \gamma_6^L + \gamma_6^R \gamma_7^R \gamma_3^L \gamma_5^L + \gamma_7^R \gamma_5^R \gamma_3^L \gamma_6^L + \gamma_5^R \gamma_6^R \gamma_3^L \gamma_7^L \\ &+ \gamma_4^R \gamma_6^R \gamma_7^L \gamma_1^L + \gamma_4^R \gamma_7^R \gamma_1^L \gamma_6^L + \gamma_4^R \gamma_1^R \gamma_6^L \gamma_7^L + \gamma_7^R \gamma_1^R \gamma_4^L \gamma_6^L + \gamma_1^R \gamma_6^R \gamma_4^L \gamma_7^L + \gamma_6^R \gamma_7^R \gamma_4^L \gamma_1^L \\ &+ \gamma_5^R \gamma_7^R \gamma_1^L \gamma_2^L + \gamma_5^R \gamma_1^R \gamma_2^L \gamma_7^L + \gamma_5^R \gamma_2^R \gamma_7^L \gamma_1^L + \gamma_1^R \gamma_2^R \gamma_5^L \gamma_7^L + \gamma_2^R \gamma_7^R \gamma_5^L \gamma_1^L + \gamma_7^R \gamma_1^R \gamma_5^L \gamma_2^L \\ &+ \gamma_6^R \gamma_1^R \gamma_2^L \gamma_3^L + \gamma_6^R \gamma_2^R \gamma_3^L \gamma_1^L + \gamma_6^R \gamma_3^R \gamma_1^L \gamma_2^L + \gamma_2^R \gamma_3^R \gamma_6^L \gamma_1^L + \gamma_3^R \gamma_1^R \gamma_6^L \gamma_2^L + \gamma_1^R \gamma_2^R \gamma_6^L \gamma_3^L \\ &+ \gamma_7^R \gamma_2^R \gamma_3^L \gamma_4^L + \gamma_7^R \gamma_3^R \gamma_4^L \gamma_2^L + \gamma_7^R \gamma_4^R \gamma_2^L \gamma_3^L + \gamma_3^R \gamma_4^R \gamma_7^L \gamma_2^L + \gamma_4^R \gamma_2^R \gamma_7^L \gamma_3^L + \gamma_2^R \gamma_3^R \gamma_7^L \gamma_4^L \\ &+ \gamma_1^R \gamma_3^R \gamma_4^L \gamma_5^L + \gamma_1^R \gamma_4^R \gamma_5^L \gamma_3^L + \gamma_1^R \gamma_5^R \gamma_3^L \gamma_4^L + \gamma_4^R \gamma_5^R \gamma_1^L \gamma_3^L + \gamma_5^R \gamma_3^R \gamma_1^L \gamma_4^L + \gamma_3^R \gamma_4^R \gamma_1^L \gamma_5^L \\ &+ \gamma_2^R \gamma_4^R \gamma_5^L \gamma_6^L + \gamma_2^R \gamma_5^R \gamma_6^L \gamma_4^L + \gamma_2^R \gamma_6^R \gamma_4^L \gamma_5^L + \gamma_5^R \gamma_6^R \gamma_2^L \gamma_4^L + \gamma_6^R \gamma_4^R \gamma_2^L \gamma_5^L + \gamma_4^R \gamma_5^R \gamma_2^L \gamma_6^L. \end{aligned} \quad (C3)$$

Appendix D: details of device realizations of $G(-\frac{\pi}{4})$,

$$G(\frac{\pi}{10}) \text{ and } G(\frac{2\pi}{5})$$

As described in the main text, by a proper arrangement of the interaction areas, the device in Fig. 3(a) of the main text can realize $G(-\frac{\pi}{4})$, $G(\frac{\pi}{10})$ and $G(\frac{2\pi}{5})$. The details are shown in Fig. 17.

Appendix E: The electric signals with phase gates

Consider the setup in Fig. 4 in the main text. The phase gate is represented by $G_{ij}(\theta) = \text{diag}(1, e^{-i2\theta}) = \text{diag}(1, e^{-i\eta})$ on the basis $|0^{\gamma_i \gamma_j}\rangle$ and $|1^{\gamma_i \gamma_j}\rangle$, where 0

and 1 labels the fermion number. Then, in the parity even basis $(|0_A 0_B 0_C\rangle, |0_A 1_B 1_C\rangle, |1_A 0_B 1_C\rangle, |1_A 1_B 0_C\rangle)^T$, the transformation matrix corresponding to Fig. 4 in the main text reads

$$\frac{1}{2} \begin{pmatrix} -(1 - e^{-i\eta_5}) & ie^{-i\eta_{12}}(1 + e^{-i\eta_5}) & 0 & 0 \\ i(1 + e^{-i\eta_5}) & e^{-i\eta_{12}}(1 - e^{-i\eta_5}) & 0 & 0 \\ 0 & 0 & e^{-i\eta_{13}}(-e^{-i\eta_4} + e^{-i\eta_{45}}) & ie^{-i\eta_{23}}(e^{-i\eta_4} + e^{-i\eta_{45}}) \\ 0 & 0 & ie^{-i\eta_{13}}(e^{-i\eta_4} + e^{-i\eta_{45}}) & e^{-i\eta_{23}}(e^{-i\eta_4} - e^{-i\eta_{45}}) \end{pmatrix} \quad (E1)$$

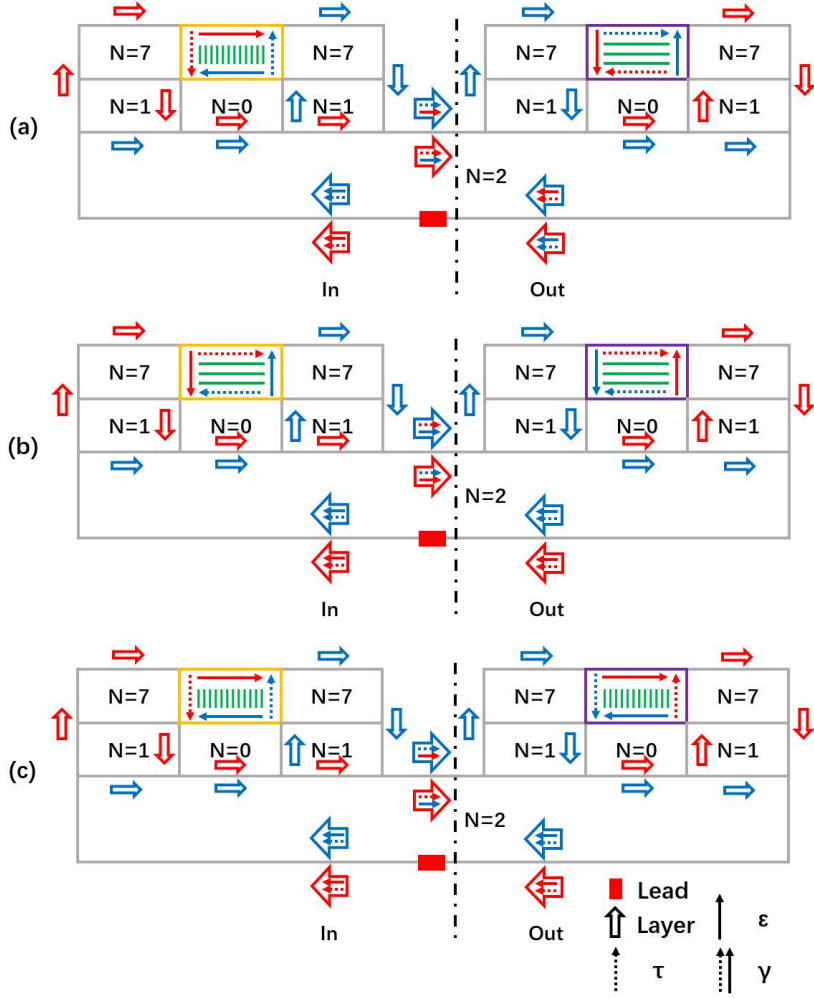


FIG. 17: (Color online) (a), (b), and (c) are the top view of the device for $G(-\frac{\pi}{4})$, $G(\frac{\pi}{10})$ and $G(\frac{2\pi}{5})$ in Fig. 3 of the main text.

where $\eta_{ij} = \eta_i + \eta_j$ and $\eta_{ijk} = \eta_i + \eta_j + \eta_k$. Notice that the conductance between Lead 2 and Lead 3 is $\sigma_{23} = (1 - |\langle \psi_f | \psi_i \rangle|^2) e^2 / h$, then if we choose the initial state $|\psi_i\rangle = |0_A 0_B 1_C\rangle$, then the final state is

$$|\psi_f\rangle = -\frac{1}{2}(1 - e^{-i\eta_5})|0_A 0_B 0_C\rangle + \frac{1}{2}[ie^{-i\eta_{12}}(1 + e^{-i\eta_5})]|0_A 1_B 1_C\rangle, \quad (\text{E2})$$

and the corresponding conductance is $\sigma_{23} = \cos^2(\theta_5) \frac{e^2}{h}$. Similar results for electric signals can be obtained for the other three initial states. Furthermore, one solution for the CNOT gate is $2\theta_1 = \frac{\pi}{2}$ and $2\theta_2 = 2\theta_3 = 2\theta_4 = 2\theta_5 = -\frac{\pi}{2}$, and they can be realized through topological $\frac{\pi}{4}$ -phase gates.

Appendix F: Details of the CNOT gate in sparse encoding

In the sparse encoding, 2-qubits are associated with 4 pairs of MEMs $(\gamma_1, \gamma_2), \dots, (\gamma_7, \gamma_8)$ labeled as A, B, C, D . If choosing the even FP input state given by $\gamma_1 \gamma_2 \gamma_3 \gamma_4 = \gamma_5 \gamma_6 \gamma_7 \gamma_8 = +1$, the basis of system is $\{|0_A 0_B 0_C 0_D\rangle, |0_A 0_B 1_C 1_D\rangle, |1_A 1_B 0_C 0_D\rangle, |1_A 1_B 1_C 1_D\rangle\}$.

We take $\gamma_{4,5}$ as an ancillary qubit and measure its FP, i.e., $i\gamma_4 \gamma_5$. Before measuring, γ_6 exchanges with $\gamma_{4,5}$ and forms a new pair with γ_3 . This equals to act $B_{45} B_{56}$ on the $\gamma_3 \gamma_4 \gamma_5 \gamma_6$ and gives superposition states

$$\begin{pmatrix} |0_A 0_B 0_C 0_D\rangle + |0_A 1_B 1_C 0_D\rangle \\ i|0_A 0_B 1_C 1_D\rangle - i|0_A 1_B 0_C 1_D\rangle \\ |1_A 0_B 1_C 0_D\rangle + |1_A 1_B 0_C 0_D\rangle \\ -i|1_A 0_B 0_C 1_D\rangle + i|1_A 1_B 1_C 1_D\rangle \end{pmatrix} \quad (\text{F1})$$

We then measure $i\gamma_4 \gamma_5$ and go ahead when it is even. This means that the fermion number of the pair C is 0,

and the remaining state is

$$\{|0_A0_B0_D\rangle, i|0_A1_B1_D\rangle, |1_A1_B0_D\rangle, i|1_A0_B1_D\rangle\},$$

which is 2-qubits for the dense encoding in odd FP.

Acting the CNOT in the dense encoding on this state, the output state is given by

$$\{|0_A0_B0_D\rangle, i|0_A1_B1_D\rangle, |1_A0_B1_D\rangle, i|1_A1_B0_D\rangle\}$$

Putting $\gamma_{4,5}$ with $i\gamma_4\gamma_5 = 1$ back, we have

$$\{|0_A0_B0_C0_D\rangle, i|0_A1_B0_C1_D\rangle, |1_A0_B0_C1_D\rangle, i|1_A1_B0_C0_D\rangle\}.$$

Braiding γ_6 with γ_4, γ_5 again, we get the superposition state

$$\left(\begin{array}{l} |0_A0_B0_C0_D\rangle - i|0_A1_B1_C0_D\rangle \\ |0_A0_B1_C1_D\rangle - i|0_A1_B0_C1_D\rangle \\ i|1_A0_B0_C1_D\rangle + |1_A1_B1_C1_D\rangle \\ i|1_A0_B1_C0_D\rangle + |1_A1_B0_C0_D\rangle \end{array} \right) \quad (\text{F2})$$

Finally we measure $\gamma_5\gamma_6\gamma_7\gamma_8$. If it is +1, we have the FP even output state in the sparse encoding

$$\{|0_A0_B0_C0_D\rangle, |0_A0_B1_C1_D\rangle, |1_A1_B1_C1_D\rangle, |1_A1_B0_C0_D\rangle\}$$

This process implements a CNOT gate in the sparse encoding with the FP even. Similarly, we can also design the CNOT gate with FP odd.

-
- [1] Y. C. Hu and C. L. Kane, *Phys. Rev. Lett.* **120**, 066801 (2018).
- [2] Y. I. Manin, *Sovetskoye Radio*, **21**, 128 (1980).
- [3] P. Benioff, *J. of Stat. Phys.* **22**, 563 (1980).
- [4] R. P. Feynman, *Int. J. Theor. Phys.* **21**, 467 (1982).
- [5] P. Shor, *Phys. Rev. A* **52**, R2493 (1995).
- [6] E. Gibney, *Nature* **574**, 22 (2019).
- [7] H.-S. Zhong et al., *Science* **370**, 1460 (2020).
- [8] J. Clarke, and F. Wilhelm, *Nature* **453**, 1031 (2008).
- [9] J. Cirac and P. Zoller, *Phys. Rev. Lett.* **74**, 4091 (1995).
- [10] M. Khazali and K. Mølmer, *Phys. Rev. X* **10**, 021054 (2020).
- [11] V. Ivády et al., *Nat. Comm.* **10**, 5607 (2019).
- [12] A. Imamoglu et al., *Phys. Rev. Lett.* **83**, 4204 (1999).
- [13] P. Neumann et al., *Science* **320**, 1326 (2008).
- [14] M. Anderlini et al., *Nature* **448**, 452 (2007).
- [15] N. Ohlsson, R. Mohan, and S. Kröll, *Opt. Comm.* **201**, 71 (2002).
- [16] B. Náfrádi et al., *Nat. Comm.* **7**, 12232 (2016).
- [17] A. Steane, *Proc. Roy. Soc. Lond. A* **452**, 2551 (1996).
- [18] S. K. Shukla, R. I. Bahar (Eds.), *Nano Quantum and Molecular Computing*, Springer US, (2004).
- [19] A. Yu Kitaev, *Ann. Phys. (NY)* **303**, 2 (2003).
- [20] S. Das Sarma, M. Freedman, C. Nayak, S. H. Simon, and A. Stern, *Rev. Mod. Phys.* **80**, (2008)1083.
- [21] E. Rowell, and Z. H. Wang, *arXiv:1705.06206*.
- [22] J. Leinaas, and J. Myrheim, *Nuovo Cimento B* **37**, 1 (1977).
- [23] F. Wilczek, *Phys. Rev. Lett.* **49**, 957 (1982).
- [24] G. Moore and N. Read, *Nucl. Phys. B* **360**, 362 (1991).
- [25] For the recent experimental progresses, see, R. L. Willett, C. Nayak, K. Shtengel, L. N. Pfeiffer, and K. W. West, *Phys. Rev. Lett.* **111**, 186401 (2013); R. L. Willett, K. Shtengel, C. Nayak, L.N. Pfeiffer, Y. J. Chung, M. L. Peabody, K. W. Baldwin, and K. W. West, *arXiv:1905.10248*.
- [26] M. Freedman et al., *Bull. Amer. Math. Soc.* **40**, 31 (2003).
- [27] N. Read and E. Rezayi, *Phys. Rev. B* **59**, 8084 (1999).
- [28] C. Nayak et al., *Rev. Mod. Phys.* **80**, 1083(2008).
- [29] R. S. K. Mong, D. J. Clarke, J. Alicea, N. H. Lindner, P. Fendley, C. Nayak, Y. Oreg, A. Stern, E. Berg, K. Shtengel, and M. P. A. Fisher, *Phys. Rev. X* **4**, 011036 (2014).
- [30] A. Vaezi, *Phys. Rev. X* **4**, 031009 (2014).
- [31] A. Y. Kitaev, *Physics-Uspekhi* **44**, 131(2001).
- [32] C. Nayak and F. Wilczek, *Nucl. Phys. B* **479**, 529 (1996).
- [33] D. A. Ivanov, *Phys. Rev. Lett.* **86**, 268 (2001).
- [34] J. Alicea, Y. Oreg, G. Refael, F. von Oppen and M. P. A. Fisher, *Nat. Phys.* **7**, 412 (2011).
- [35] L. Fu and C. L. Kane, *Phys. Rev. Lett.* **100**, 096407 (2008).
- [36] Jay D. Sau et al., *Phys. Rev. Lett.* **104**, 040502 (2010).
- [37] R. M. Lutchyn, J. D. Sau, and S. Das Sarma, *Phys. Rev. Lett.* **105**, 077001 (2010).
- [38] X. J. Luo et al., *arXiv:1803.02173*.
- [39] V. Mourik et al., *Science* **336**, 1003 (2012).
- [40] M. T. Deng et al., *Nano Lett.* **12**, 6414 (2012).
- [41] A. Das et al., *Nat. Phys.* **8**, 887 (2012).
- [42] H. O. H. Churchill et al., *Phys. Rev. B* **87**, 241401(R) (2013).
- [43] M. T. Deng et al., *Sci. Rep.* **4**, 7261 (2014).
- [44] E. J. H. Lee et al., *Nat. Nanotech.* **9**, 79 (2013).
- [45] S. Nadj-Perge et al., *Science* **346**, 602 (2014).
- [46] J.-P. Xu, M.-X. Wang, Z. L. Liu, J.-F. Ge, X. J. Yang, C. H. Liu, Z. A. Xu, D. D. Guan, C. L. Gao, D. Qian, Y. Liu, Q.-H. Wang, F.-C. Zhang, Q.-K. Xue, and J.-F. Jia, *Phys. Rev. Lett.* **114**, 017001 (2015).
- [47] H. H. Sun et al., *Phys. Rev. Lett.* **116**, 257003 (2016).
- [48] H. Zhang et al., *Nature* **556**, 74 (2018).
- [49] H. Zhang et al., *arXiv:2101.11456*.
- [50] L. Kong et al., *Nat. Phys.* **15**, 1181 (2019).
- [51] C. Chen et al., *Nat. Phys.* **16**, 536 (2020).
- [52] Z. Wang et al., *Science* **367** 104 (2020).
- [53] C. Chen et al., *Chin. Phys. Lett.* **36**, 057403 (2019).
- [54] P. Zhang et al., *Nat. Phys.* **15**, 41 (2019).
- [55] W. Liu et al., *Nat. Comm.* **11**, 5688 (2020).
- [56] C. Li, X.-J. Luo, L. Chen, D. E. Liu, F.-C. Zhang, and

- X. Liu, arXiv: 2107.11562.
- [57] Howon Kim et al., *Science Advances* **4**, eaar5251 (2018).
- [58] A. Palacio-morales et al., *Science Advances* **5**, aav6600 (2019).
- [59] L. Schneider, P. Beck, J. Wiebe, and R. Wiesendanger, *Science Advances* **7**, abd7302 (2021).
- [60] C.-K. Chiu, T. Machida, Y. Y. Huang, T. Hanaguri, and F.-C. Zhang, *Sci. Adv.* **6**, eaay0443 (2020).
- [61] N. Read and D. Green, *Phys. Rev. B* **61**, 10267 (2000).
- [62] K. Ishida et al., *Nature* **396**, 658 (1998).
- [63] A. Pustogow et al., *Nature* **574**, 72 (2019).
- [64] X.-L. Qi, T. L. Hughes, and S.-C. Zhang, *Phys. Rev. B* **82**, 184516 (2010).
- [65] B. Lian, X.-Q. Sun, A. Vaezi, X.-L. Qi, and S.-C. Zhang, *PNAS* **115**, 10938 (2018).
- [66] J. C. Budich, S. Walter, and B. Trauzettel, *Phys. Rev. B*, **85**, 121405(R) (2012).
- [67] N. Breckwoldt, T. Posske and M. Thorwart, *New J. Phys.*, **24**, 013033 (2022).
- [68] Q. L. He, L. Pan, A. L. Stern, E. C. Burks, X. Y. Che, G. Yin, J. Wang, B. Lian, Q. Zhou, E. S. Choi, K. Murata, X. F. Kou, Z. J. Chen, T. X. Nie, Q. M. Shao, Y. B. Fan, S.-C. Zhang, K. Liu, J. Xia, and K. L. Wang, *Science* **357**, (2017)294.
- [69] W. J. Ji, and X.-G. Wen, *Phys. Rev. Lett.* **120**, 107002 (2018).
- [70] M. Kayyalha, D. Xiao, R. X. Zhang, J. H. Shin, J. Jiang, F. Wang, Y.-F. Zhao, R. Xiao, L. Zhang, K. M. Fijalkowski, P. Mandal, M. Winnerlein, C. Gould, Q. Li, L. W. Molenkamp, M. H. W. Chan, N. Samarth, C.-Z. Chang, *Science* **367**, 64 (2020).
- [71] A. Stern and B. I. Halperin, *Phys. Rev. Lett.* **96**, 016802 (2006).
- [72] P. Bonderson, A. Kitaev, and K. Shtengel, *Phys. Rev. Lett.* **96**, 016803 (2006).
- [73] N. R. Ayukaryana, M. H. Fauzi, and E. H. Hasdeo, *AIP Conf. Proc.* **2382**, 020007 (2021).
- [74] C.W. J. Beenakker, P. Baireuther, Y. Herasymenko, I. Adagideli, L. Wang, and A. R. Akhmerov, *Phys. Rev. Lett.* **122**, 146803 (2019).
- [75] S. Shatashvili and C. Vafa, *Sel. Math. Sov.* **1**, 347 (1995).
- [76] H. Bartolomei, M. Kumar, R. Bisognin, A. Marguerite, J.-M. Berroir, E. Bocquillon, B. Placais, A. Cavanna, Q. Dong, U. Gennser, Y. Jin, and G. Fève, *Science* **368**, 173 (2020).
- [77] P. Di Francesco, P. Mathieu and D. Senechal, *Conformal Field Theory, 1997, Springer-Verlag, New York, Inc.*
- [78] P. O. Boykin, T. Mor, M. Pulver, V. Roychowdhury, and F. Vatan, *Info. Proc. Lett.* **75**, 101 (2000).
- [79] A. Barenco, C. H. Bennett, R. Cleve, D. P. DiVincenzo, N. Margolus, P. Shor, T. Sleator, J. A. Smolin, and H. Weinfurter, *Phys. Rev. A* **52**, 3457 (1995).
- [80] S. D. Sarma, M. Freedman, and C. Nayak, *npj Quan. Inf.* **1**, 15001 (2015).
- [81] S. Bravyi, *Phys. Rev. A* **73**, 042313(2006).
- [82] P. R. Hammar, B. R. Bennett, M. J. Yang, and M. Johnson, *Phys. Rev. Lett.* **83**, 203 (1999).
- [83] T. Fukumoto, K. Taguchi, S. Kobayashi, and Y. Tanaka, *Phys. Rev. B* **92**, 144514 (2015).
- [84] J. Zelezny, Y. Zhang, C. Felser, and B. Yan, *Phys. Rev. Lett.* **119**, 187204 (2017).
- [85] T. Y. Chen, Z. Tesanovic, and C. L. Chien, *Phys. Rev. Lett.* **109**, 146602 (2012).
- [86] C. W. J. Beenakker, D. P. DiVincenzo, C. Emary, and M. Kindermann, *Phys. Rev. Lett.* **93**, 020501 (2004).
- [87] D. Deutsch, *Proc. Roy. Soc. London Ser. A* **400**, 97 (1985).
- [88] M. A. Nielsen and I. L. Chuang, *Quantum Computation and Quantum Information*, Cambridge University Press, 2000.
- [89] V. Vedral, A. Barenco, and A. Ekert, *Phys. Rev. A* **54**, 147 (1996).
- [90] O. Zilberberg, B. Braunecker, and D. Loss, *Phys. Rev. A* **77**, 012327 (2008).
- [91] For a recent review, see S. S. Gill et al., accepted for publication in "Software: Practice and Experience", Wiley Press, USA, 2021. (arXiv 2010.15559)
- [92] J. C. Baez, *Bull. Am. Math. Soc.* **39**, 145 (2002).
- [93] M. Günaydin and S. V. Ketov, *Nucl. Phys. B* **467**, 215 (1996).